Bulk exocytosis of large intracellular apical precursor organelles establishes apical domain identity during *de novo* lumen formation

Eleanor Martin[1,2,#], Sujasha Ghosh[1,2,#], Yuhong Chen[1,2], Rossana Girardello[4], Barbara Hübner[1,2], Kay En Low[3], Gunnar Dittmar[4,5,*], and Alexander Ludwig[1,2,6,*]

[1] School of Biological Sciences, Nanyang Technological University, 60 Nanyang Drive, Singapore 637551
[2] NTU Institute of Structural Biology (NISB), Nanyang Technological University, 59 Nanyang Drive, Singapore 636921
[3] Electron Microscopy Unit, Yong Loo Lin School of Medicine, National University of Singapore (NUS), Singapore
[4] Proteomics of Cellular Signaling, Luxembourg Institute of Health, 1a Rue Thomas Edison, 1445 Strassen, Luxembourg
[5] Department of Life Sciences and Medicine, University of Luxembourg, 4365 Esch-sur-Alzette, Luxembourg

[6] Lead contact

* correspondence: aludwig@ntu.edu.sg; gunnar.dittmar@lih.lu

[#] these authors contributed equally

Abstract
The creation of a microvilli-rich apical luminal domain is a key event in the development of epithelial tissues. *De novo* lumenogenesis, in which epithelial cells establish apical identity by directing apical cargo to an apical membrane initiation site (AMIS), has been studied extensively. However, the mechanisms that govern the formation of the AMIS and its progression into a luminal precursor remain poorly understood. In this study, we employed super-resolution imaging, light and electron microscopy, and time-resolved proximity proteomics to explore the spatial, temporal, and molecular processes involved in apical lumen initiation in MDCK-II cells. Interestingly, we discovered that, in both 2D and 3D cultures, the formation of the apical cell cortex begins with the fusion of large intracellular apical precursor organelles called vacuolar apical compartments (VACs) at developing cell junctions. Time-resolved proteomics and high-resolution imaging indicate that the exocytosis of VACs and lumen initiation is temporally coordinated with the formation and maturation of the apical junctional complex. Furthermore, we report that loss of the Crumbs complex proteins Pals1 or PatJ perturbs the organisation of the apical cell cortex and impedes VAC exocytosis at the AMIS, resulting in severe defects in lumen morphogenesis. Overall, our findings define a temporally resolved protein network for *de novo* cell polarization and highlight Pals1/PatJ as key regulators of apical domain initiation. We further propose that VACs represent a previously unrecognized apical transport carrier that plays a crucial role in the rapid establishment of apical domain identity.

Introduction
The formation of luminal epithelial structures is critical during development and a central feature of many organs. Lumens and tubes can be formed through a variety of mechanisms, yet all tubular organs share a common feature: they are built of sheets

of polarized epithelial cells that orient their apical surface towards a central lumen [1-6]. Aberrations in lumen formation or maintenance can lead to developmental disorders such as those seen in certain kidney and intestinal diseases.

De novo lumen formation refers to the development of an apical lumen in the centre of a group of polarizing cells. Lumen initiation can be achieved through cavitation, which is mediated by apoptotic cell death, or through cord hollowing, which relies on the transport of apical determinants to an apical membrane initiation site. Cord hollowing is utilized for lumenogenesis in the vertebrate kidney [7-9], the zebrafish gut [10,11], and the mammalian blastocyst [12-14]. Madin-Darby Canine Kidney type II cells (MDCK-II, henceforth referred to as MDCK) also form luminal cysts via cord hollowing when cultured in Matrigel [15]. Lumenogenesis in MDCK cells is highly stereotypic and temporally well-defined, and many mechanisms first demonstrated in this system have subsequently been shown to operate *in vivo* [1-6,15]. MDCK cells therefore offer a powerful 3D cell culture model to study *de novo* apical lumen formation.

Central to *de novo* lumenogenesis is the assembly of an apical membrane initiation site (AMIS) and its subsequent maturation into a luminal precursor, the pre-apical patch (PAP). The AMIS is a transient and universal lumen-initiating structure [8,9,16-18], yet how the AMIS matures into an apical luminal surface is not clear. In MDCK cells the AMIS is formed at the cytokinetic furrow (or midbody) after the first cell division. The site of AMIS assembly is specified by specific phospholipids and polarity factors such as Par3, leading to local Rho GTPase signaling and rearrangements in the actin cytoskeleton [16,19-21]. Apical membrane proteins (such as Crumbs-3 (Crb3) and podocalyxin (PODXL)) are then internalized from the ECM-facing cortex and delivered to the AMIS via vesicular transport. Current models imply that transcytosis of apical cargo is mediated by apical Rab GTPases including Rab11, Rab8, Rab3, and Rab35 [16,22-25]. Once apical cargo has been delivered, the AMIS transforms into the PAP. The formation of the PAP is characterized by the assembly of tight junctions (TJs) and adherens junctions (AJs) around the nascent apical surface. In a final step opposing apical membranes create a nascent lumen, which expands and grows in volume as cells in the cyst divide. Opening and growth of the lumen has been suggested to be mediated by electrostatic repulsion of charged apical membrane proteins (such as PODXL) and by apical proton pumps that establish electrochemical gradients leading to fluid influx into the lumen [10,26,27]. This illustrates that *de novo* lumen formation is a hierarchical process that relies on the precise temporal coordination of membrane trafficking, cell-cell junction formation and apical domain specification and growth. However, the underlying molecular mechanisms that regulate the formation of the AMIS and its transition into the PAP are not well understood, in part because spatio-temporal and ultrastructural information of the lumen initiation process is limited, even in the MDCK cell system.

In this study, we investigated the dynamics and ultrastructural underpinning of lumen initiation in MDCK cells with a focus on the epithelial Crumbs complex, a key and evolutionarily conserved regulator of epithelial tissue morphogenesis [28,29]. The Crumbs complex is composed of the transmembrane protein Crb3, the adaptor proteins Pals1, and the multi-PDZ domain scaffolding protein PatJ. In mice, the loss of *Crb3* or *Pals1* disrupts tissue architecture in multiple organs, including the intestine, lung, and kidney [30-32]. Similarly, in MDCK cells, silencing or inactivation of Crb3, Pals1, or PatJ impairs TJ assembly and results in a multi-lumen phenotype, where multiple ectopic lumens form instead of a single apical lumen [33-40]. However, how and at which stage of lumenogenesis the Crumbs complex functions is unclear.

By combining light and electron microscopy with time-resolved proximity proteomics, we demonstrate that apical lumen initiation is temporally and spatially coordinated with the assembly of the apical junctional complex (AJC). Unexpectedly, we also discovered that apical cargo is delivered to the AMIS via large intracellular organelles known as vacuolar apical compartments (VACs), which fuse with the AMIS to initiate apical domain identity. Furthermore, we show that PatJ and Pals1 are essential for VAC exocytosis, and consequently, for proper lumen initiation at the AMIS/PAP stage.

Results

Pals1 and apical cargo are delivered to nascent cell-cell contacts via VACs

Using proximity labeling proteomics and transmission electron microscopy (TEM) with the peroxidase APEX2 [41] we previously demonstrated that the Crumbs complex forms a distinct domain apical of TJs, the so-called vertebrate marginal zone (VMZ) [39]. The spatial separation of the Crumbs complex from apical cell junctions is evolutionarily conserved [42], suggesting a specific role at the apical-lateral interface. We set out to study the spatio-temporal assembly of the VMZ using a stable MDCK-II cell line expressing a Pals1-APEX2-EGFP (Pals1-A2E) fusion protein. The well-established calcium switch model was used to determine the localization of Pals1 at distinct stages of cell-cell junction formation by light microscopy and TEM. In addition, we used the Pals1-A2E protein as a proxy to study the assembly and maturation of the apical-lateral border using time-resolved proximity proteomics.

In fully confluent MDCK cells Pals1-A2E was localised at apical cell junctions, as expected. Time lapse microscopy revealed that ~6h after calcium depletion Pals1 started to coalesce at the cell membrane, followed by its internalization into large intracellular vacuoles that appeared to fuse with each other in the cell cytoplasm (Figure 1A). Such vacuoles have previously been described as vacuolar apical compartments (VACs) [43,44]. In agreement with earlier data, VACs contained apical proteins (e.g. ezrin) and were enriched in F-actin (Figure S1A). Previously identified VMZ proteins (PatJ, Homers, and ArhGAP29) were also localised to VACs, whereas TJ proteins (ZO-1, Par3) were not and instead formed small puncta in the cytoplasm. In addition, VACs were strongly labeled by the calcium binding dye Fluo-4 and contained the apical calcium pump PMCA2-w/b (Figure S1B and S1C). When calcium-depleted cells were shifted back to normal calcium media, VACs progressively disappeared and were no longer detectable 6h post calcium replenishment (Figure 1B). At the same time, TJs reformed, resulting in a continuous TJ belt by 6h. Quantification revealed an inverse relationship between the number of VACs and TJ length (determined by ZO-1 labeling) during junction establishment (Figure 1C), indicating that VAC exocytosis and TJ formation are temporally coordinated.

To understand when and where VACs are exocytosed, we analysed the localization of PODXL, a well-characterised apical glycoprotein, at different stages of the calcium switch assay (Figure 1D). In calcium-depleted cells (0h), PODXL and F-actin (stained with phalloidin) were highly enriched in VACs (Figure 1D, left panel), as expected. At 2h post calcium addition, apparent VAC exocytosis and nascent VAC fusion events with the lateral membrane were evident (Figure 1D, middle panel, and Figure S1F), in agreement with previous data [43]. In addition, we noted the presence of elongated, F-actin rich and PODXL-containing pockets along the lateral membrane (Figure 1D, right panel). Such pockets displayed an apparent paracellular space,

suggesting the formation of a lateral lumen. Interestingly, staining of ZO-1 and PatJ revealed that VAC fusion sites and nascent lateral lumens were surrounded by a junctional ring (Figure 1E). We concluded that VACs deliver apical cargo to nascent cell-cell contacts to initiate the assembly of a lateral lumenal space.

VACs are exocytosed at nascent cell-cell contacts

Next, we analysed the ultrastructure of VACs and the dynamic sub-cellular redistribution of Pals1 during cell-cell junction assembly using APEX2-TEM. Pals1-A2E MDCK cells were fixed at 0h, 2h, and 6h of the calcium switch assay and subjected to APEX2 labeling (Figure 2A). The APEX2 tag serves as an electron-dense label, permitting proteins to be localised with 5-10 nm precision [45]. In calcium-depleted cells, VACs appeared as large intracellular vacuoles rich in apical microvilli (Figure 2B (0h) and Figure S1D). Microvilli often appeared more electron dense than the surrounding membranes, indicating the presence of Pals1 (Figure 2B (0h), black arrowheads). VACs were frequently surrounded by small vesicles (Figure 2B (0h), white arrowheads). Golgi cisternae were also observed in proximity to the VACs (Figure S1D). At 2h post calcium addition, fusion events of VACs with the lateral membrane were evident (Figure 2B (2h) and Figure S1E). The fusion pore was clearly visible. In addition, open microvilli-rich lumens were observed at the lateral domain (Figure 2B (2h) and Figure S1E). Moreover, Pals1 labeling was observed at cell-cell contacts immediately adjacent to the VAC fusion pores and lateral lumens. These TEM micrographs correlate with the data shown in Figure 1D and 1E and show that VACs indeed fuse with the lateral membrane.

To analyse the ultrastructure of VAC fusion sites and lateral lumens in more detail, we performed a comprehensive serial section TEM analysis of Pals1-A2E MDCK cells 2h post calcium addition. Embedded cell monolayers were sectioned parallel to the growth support (glass coverslip), producing consecutive *en face* TEM sections spanning ~5 µm of cell volume (Figure 2A). Serial section TEM of nascent VAC fusion sites revealed a strong electron-dense label above (apical), below (basal), and adjacent to the fusion pore (Figure 2C). This indicates that upon fusion of the VAC with the lateral membrane, Pals1 rapidly accumulates at nascent cell-cell contacts. Lateral lumens containing microvilli were also surrounded by cell-cell junctions labeled by Pals1 (Figure 2D and Figure S1G). Labeling was again evident both apical and basal of the lumen opening. This demonstrated that VACs fuse at nascent cell junctions and that Pals1 forms a junctional ring around the developing lateral lumen. Lastly, serial section TEM of Pals1-A2E MDCK cell monolayers 6h post calcium addition (a time point at which cell junctions are fully assembled) revealed Pals1 labeling apical of the AJC (Figure 2E). TEM of monolayers imaged in cross-sections confirmed that Pals1 is restricted to the VMZ once cell junctions have formed and apico-basal polarity has been established (Figure 2B (6h)). We concluded that VAC exocytosis at nascent cell junctions leads to the initiation of a luminal surface at the lateral membrane interface. This is followed by the formation and maturation of the AJC and the spatial separation of the VMZ and TJs (Figure 2F).

A time-resolved proximity proteome uncovers a dynamic protein network during cell-cell junction assembly

We wanted to understand the molecular basis of the complex ultrastructural rearrangements that occur during the assembly and maturation of the AJC. To this end we generated proximity proteomes of Pals1-A2E at distinct stages of the calcium switch assay (Figure 3 and Figure S2). APEX2 proximity biotinylation was carried out

at 0h, 0.5h, 2h, 4h, and 6h following previously established protocols [39,46] (Figure 3A). Cells expressing NES-A2E and non-biotinylated samples of the Pals1-A2E cell line were used as controls. Principal Component Analysis showed a strong correlation between replicates of the same time point, and early and late time points were clearly separated from each other (Figure S2A). After removal of common contaminants and proteins that were not significantly enriched with Pals1 compared to the controls, we arrived at a proteome of 278 proteins (Figure S2B). These proteins were significantly enriched in at least one of the five time points measured, allowing us to quantify their relative abundance at each time point. The 278 proteins dataset was subjected to unsupervised hierarchical clustering, resulting in four clusters with distinct kinetics (Figure 3B and 3C and Figure S2C and S2D). Cluster 4 contained proteins that were rapidly depleted from the Pals1 proteome upon calcium addition, cluster 1 and cluster 2 contained proteins that became transiently enriched at 0.5h and 2h, respectively, and cluster 3 contained proteins whose log2 fold changes progressively increased, reaching peak enrichment at 6h (Figure 3B and 3C). Gene Ontology analysis showed that clusters 1 and 2 were enriched in proteins associated with protein transport and GTPase signaling, whilst cluster 3 was enriched in proteins involved in cell-cell adhesion and the regulation of the actin cytoskeleton (Figure S2E). Moreover, cluster 3 was enriched in proteins previously identified in a static Pals1 proximity proteome determined from fully polarized MDCK cell monolayers (Figure S2F) [39].

To visualise the molecular composition, connectivity and temporal evolution of the Pals1-associated protein network, we generated a temporally resolved protein-protein interaction network based on STRING and BioGRID database entries (Figure 3D). For simplicity, only 200 out of the 278 proteins identified were used for this analysis (cytosolic, ribosomal, and miscellaneous proteins were not considered). Proteins were grouped according to established functions and based on our previous proteomics analysis of the apical-lateral border [39]. Cluster 4 contained proteins involved in calcium binding and signaling (annexins), suggesting that such proteins dissociate from VACs soon after extracellular calcium replenishment. Cluster 1 contained all major Rho-type GTPases (RhoA, RhoC, Rac1, and Cdc42) and regulators of the actin cytoskeleton including actin assembly factors (e.g. VASP, ARPC3, NCK1, GSN, WDR1), capping proteins (e.g. CAPG, CAPZA1), and myosin-II motor subunits (MYL6, MYL12B). In addition, Rab and SNARE proteins involved in apical trafficking (Rab11B, Rab25, Rab3D) and endosomal transport (Rab5B, Rab5C, SNX3, STX12, STX7) were present in cluster 1. Light microscopy and TEM of APEX2 fusion proteins showed that Rab3, Rab11, and Rab25 are associated with vesicles surrounding the VACs, whereas Rab35 specifically labeled microvilli facing the VAC lumen (Figure S3). This validates our proteomics data and suggests a role of these Rabs in the trafficking of apical cargo to the VACs. Cluster 2 encompassed proteins that became enriched with Pals1 at 0.5-2h. Unlike proteins in cluster 1 (which peaked at 0.5h and became de-enriched after 4h), those in cluster 2 remained associated with Pals1 until 6h of the calcium switch. Interestingly, this cluster contained integral membrane proteins of the TJ (F11R (JAM-A), CLDN1 (claudin-1) and CLDN4 (claudin-4)) as well as RhoG and Rap1A. The Ras-type GTPases KRAS, NRAS, RRAS, RRAS2 and RALA were also enriched in cluster 2. We then examined cluster 3, i.e. proteins that were highly enriched at late stages of the calcium switch (at 2-6 h). This cluster contained VMZ components (MPP5/Pals1, PATJ, PKN2 and PTPN13), TJ scaffolding proteins (TJP1 (ZO-1), TJP3 (ZO-3), PARD3 (Par3), PRKCI (atypical PKC), CGN (cingulin)), apical membrane proteins (PODXL, MUC1, CD44), and the ERM proteins EZR (ezrin), RDX (radixin), and MSN (moesin). In addition, Rap2C and

components of the junctional actin cortex (e.g. LIMA1 (eplin), ZYX (zyxin), ACTN4 (alpha-actinin 4), WASL (N-WASP), FNBP1L (TOCA-1)) were enriched at mature cell junctions. Figure 3E summarizes the distinct kinetics of Rho and Ras GTPases and the step-wise assembly of the AJC, with TJ membrane proteins becoming enriched at 0.5h followed by TJ scaffolding and VMZ proteins at 2h. Interestingly, apical proteins did not become enriched with Pals1 until 4h of the calcium switch (Figure 3F), suggesting that the VMZ separates from TJs (and hence moves closer to the apical cortex) at around this time. We concluded that the assembly and maturation of the AJC is a hierarchical process that is driven by extensive molecular remodeling of the junctional proteome. In addition, the temporally resolved protein interaction network mirrors the subcellular dynamics of Pals1 during cell junction assembly visualized by TEM.

VACs are formed during lumen formation in MDCK 3D cultures

Our data from the calcium switch assay indicated that VAC exocytosis at nascent cell contacts leads to the formation of a lateral lumen surrounded by cell-cell junctions. To study this process in a more physiological context, we analysed lumen initiation in the MDCK 3D cyst assay. In mature MDCK cysts PatJ (and Pals1, not shown) localised to apical cell junctions, whilst ezrin labeled the apical cortex (Figure 4A). Airyscan imaging revealed that PatJ localizes apical of ZO-1 (Figure 4B), in line with previous work [38,39,47]. To understand when the VMZ and TJs separate from each other, we analysed the localization of VMZ and TJ proteins at early stages of lumen initiation. At the early (inverted) 2-cell stage (~16h in Matrigel), Pals1, PatJ, and ZO-1 localised at the cell-cell interface (Figure 4C and 4D), whilst at the PAP stage (20-24h in Matrigel) these proteins formed discrete puncta surrounding the nascent apical lumen (Figure 4E and 4F). Line scans revealed a perfect overlap between Pals1 and PatJ (Figure 4G). By contrast, ZO-1 and PatJ were offset by ~150 nm, with PatJ localising more apical than ZO-1 (Figure 4H). Homer proteins, which interact directly with PatJ [39], colocalised with Pals1 and PatJ both at the inverted and PAP stages (Figure S4A and S4B) as well as in mature cysts (not shown). This indicated that the initiation of apical domain identity is tightly coordinated with the assembly and spatial separation of TJs and the VMZ.

Next, we examined the spatio-temporal localization of PatJ in relation to the apical marker ezrin. MDCK cells embedded in Matrigel were fixed between 16h and 24h and stained for PatJ and the apical marker ezrin. At the inverted cell stage (~16-20h), ezrin was localised to the ECM-facing membrane, whilst PatJ was either localised along the cell-cell contact zone or formed discrete puncta at the distal ends of the cell-cell contact interface (Figure 4I). At ~20h, ezrin was largely depleted from the ECM-facing membrane and instead localised to large (1-2 µm) intracellular vacuoles, which appeared as rings with a hollow center, highly reminiscent of VACs (Figure 4J). Interestingly, structures of similar appearance and size were also found in close association with the AMIS marked by PatJ (Figure 4J and 4K), suggesting that such vacuoles fuse with the AMIS. Lastly, at 24h, most cell doublets displayed a PAP/nascent lumen phenotype, with ezrin clearly being enriched apically and PatJ puncta surrounding the lumen (Figure 4L). This shows that PatJ accumulates at the AMIS prior to or concomitantly with the arrival of apical cargo.

To ascertain that the vacuolar structures observed during the AMIS-PAP transition were indeed VACs, we processed MDCK cells grown for 18h in Matrigel for TEM. Both *en face* and cross-sections through cell doublets were obtained. Interestingly, most cell doublets exhibited interdigitated cell-cell contacts with a high

density of finger-like protrusions (Figure S5A), likely corresponding to E-Cadherin-based adhesions [48]. In addition, electron-dense cell-cell contacts reminiscent of TJs were observed at the ECM-facing ends of the cell-cell contact interface (Figure S5B). Importantly, 1-2 µm size intracellular vacuoles containing apical microvilli were readily identified (Figure 5A). These structures appeared identical to VACs observed in calcium switch assays. Moreover, microvilli-rich membrane pits were observed at the ECM-facing plasma membrane (Figure 5A). To support these findings, we imaged PAP/early lumen stages using focused-ion-beam SEM (FIB-SEM) (Figure 5B-5D and Figure S6), which offered 3D ultrastructural information of the cell doublet at a resolution of 10x10x30 nm. Inspection of the available EM volume revealed that both cells of the cell doublet contained at least one VAC (Figure 5B, slice 1 and 188). The VACs were intracellular, i.e. not continuous with the apical lumen (Figure 5C and Movie S1). In addition, and in support of our TEM analysis, several membrane invaginations enriched in microvilli were observed at the ECM-facing plasma membrane (Figure 5B, slice 42 and 130, Figure 5D, Figure S6A, slice 201 and 294, and Movies S2-S5). Based on their unique ultrastructure, we propose that such membrane pits represent sites of apical membrane internalization. We further note that rather than forming one large apical lumen, the apical surface appeared as a network of “mini-lumens” interrupted by cell-cell junctions (Figure S6B). We concluded that VACs are a characteristic feature of *de novo* lumen formation in MDCK 3D cultures that deliver apical cargo to the AMIS.

VACs fuse with the AMIS

Our data suggested that VACs arise through the internalization of microvilli-enriched membrane from the ECM-facing plasma membrane. To test this directly, we analysed PODXL trafficking using an antibody uptake assay. PODXL antibody was added to MDCK cells at 16h in Matrigel and washed out at 18h. Cells were fixed at defined time intervals (18h, 20-22h and 24h) and costained with phalloidin to visualize F-actin (Figure 6A and Figure S7). As expected, at 18h PODXL was largely confined to the ECM-facing plasma membrane whilst F-actin was enriched at the cell-cell contact interface. At 20-22h PODXL was found in small vesicular structures and in large (~1-2 µm in size) hollow vacuoles in the cell cytoplasm that were also stained by phalloidin. Apparent fusion events of such vacuoles with the AMIS were also observed at this time point. At 24h PODXL was enriched at the nascent luminal domain, as expected. Interestingly, uptake experiments further showed that fluorescently conjugated Wheat Germ Agglutinin (WGA), which has a high affinity for sialic acid and N-acetylglucosamine modified glycoproteins, was conspicuously absent from PODXL-labeled vacuoles (Figure S7A), but partially colocalised with PODXL in small vesicular structures (Figure S7B). This indicates specificity and selectivity in VAC-dependent cargo transport. We concluded that at least a fraction of PODXL is internalized from the ECM-facing membrane into large VAC-like organelles that are subsequently transported to and fuse with the AMIS.

To visualize potential VAC fusion events with the AMIS at higher resolution, we used correlative light and electron microscopy (CLEM). MDCK cells embedded in Matrigel for 24h were aldehyde-fixed and stained by osmium tetroxide/tannic acid impregnation. We found that this staining procedure produced a strong electron-dense stain at the lateral but not the apical membrane. This allowed us to clearly discriminate between AMIS and PAP stages as well as to identify sites of apical domain identity without relying on genetically encoded EM probes. Cell doublets in the inverted, AMIS, PAP and early lumen stages were identified by transmitted light microscopy and

subsequently imaged using serial section TEM (Figure 6B-6E). VAC-like structures were observed in the inverted cell doublet and in the AMIS stages (Figure 6B and 6C and Figure S8A). In addition, an apparent fusion event of a VAC with the AMIS was observed (Figure 6C). The fusion site appeared to be confined by cell junctions, which separated the VAC from the strongly stained and interdigitated lateral membrane. Similarly, cell doublets in the PAP and early lumen stages showed strong EM contrast at the lateral membrane whilst the microvilli-rich apical surface was not labeled (Figure 6D and 6E). Cell junctions again separated the two compartments. Analysis of serial sections confirmed that VAC fusion sites and nascent lumens are surrounded by cell junctions, which appeared as electron-lucent and flattened membranes distinct from the electron-dense and interdigitated lateral membranes (Figure S8B). This suggests that cell junction formation occurs concomitantly with or just prior to the arrival of VACs at the AMIS. Taken together our EM analysis provides strong evidence that VACs act as intracellular precursors for apical membrane initiation at the AMIS.

PatJ controls VAC exocytosis at the AMIS and apical lumen formation via the actin cytoskeleton

Our data showed that PatJ becomes enriched at the AMIS prior to or concomitantly with the delivery of VACs (Figure 4). We therefore explored whether PatJ is required for VAC exocytosis at the AMIS. To address this, we generated PatJ CRISPR/Cas9 MDCK knockout (KO) cells using sgRNAs targeting the PDZ3 and PDZ4 domains of the canine *PatJ* gene (Figure S9A-S9C). DNA sequencing revealed a 247 bp insertion in exon 11 in all clones analysed, resulting in a premature stop codon just downstream of the PDZ3 domain (Figure S9C). Western blotting and immunofluorescence confirmed that PatJ expression was lost in PatJ KO cells (Figure 7A and Figure S9D). Pals1 expression was reduced by a ~50% in PatJ KO cells, whilst ZO-1 and Par3 protein levels were unchanged (Figure 7A and Figure S9D and S9E). In line with previous reports [38,40], loss of PatJ significantly reduced bicellular ZO-1 levels and caused ZO-1 to accumulate in puncta close to tricellular junctions (Figure S9F).

We then proceeded to analyse lumen formation in WT and PatJ KO cells. Loss of PatJ resulted in a severe and fully penetrant multi-lumen phenotype, i.e. nearly 100% of MDCK KO cysts analysed showed multiple lumens instead of a single central lumen (Figure 7B and 7C). Pals1 KO cells also displayed a severe multi-lumen phenotype, in line with previous work [34,40]. To test whether the multi-lumen phenotype arises from defective lumen initiation at the 2-cell stage, we analysed MDCK cells at 24h in Matrigel using Airyscan imaging (Figure 7D) and 3D Structured Illumination Microscopy (3D-SIM) (Figure 7E). As expected, WT MDCK cells displayed a clear PAP stage pattern, with ezrin being enriched at the nascent apical lumen. By contrast, in Pals1 and PatJ KO cell doublets ezrin was found at the ECM-facing plasma membrane as well as in large intracellular vacuoles. In addition, ectopic and possibly intracellular lumens were observed. We concluded that the loss of Pals1 or PatJ impairs VAC exocytosis at the AMIS, resulting in intracellular accumulation of apical cargo and mislocalised apical lumens.

There is ample evidence that the Crumbs complex controls Rho/ROCK signaling and actomyosin contractility at the apical-lateral border [40,49-54]. Moreover, loss of Pals1 in MDCK cells has been shown to reduce junctional RhoA levels [40], suggesting that the defects in VAC exocytosis observed in Pals1 and PatJ KO cells may be due to defective Rho/ROCK signaling. To test this, we performed PODXL antibody uptake assays in the absence or presence of the Rho inhibitor Rhosin (Figure 7F). Interestingly, whilst PODXL was trafficked to the apical lumen in MDCK WT control

cells, Rho inhibition resulted in the accumulation of PODXL-containing VACs in the cytoplasm and at the AMIS, as well as in the formation of ectopic or mislocalised lumens at the 3-4 cell stage. Inhibition of ROCK (using Y-27632) or myosin-II (using Blebbistatin) caused a similar phenotype (Figure 7G). This indicates that Rho/ROCK signaling is required for normal lumen initiation.

To test whether the apical actin cytoskeleton is altered in PatJ KO cells, we co-cultured MDCK WT and PatJ KO cells on Transwell filters, which permits direct side-by-side comparison of cellular features. Phalloidin staining on mature and fully polarized monolayers clearly demonstrated that apical F-actin levels are drastically reduced in PatJ KO cells compared to WT cells (Figure 8A and 8B). In addition, scanning EM of the apical cell surface of mature MDCK WT monolayers revealed a dense network of microvilli that appeared to form a dome-like structure in the center of the apical domain (Figure 8C). By contrast, in PatJ KO cells apical microvilli were sparser and the apical cell surface appeared flattened. Moreover, and interestingly, in WT cells transjunctional protrusions were evident, which spanned the apical margins of neighbouring cells. Such “marginal cross-bridges” were less frequent and less pronounced in PatJ KO cells and likely represent intermicrovillar adhesion complexes previously described in intestinal epithelia [55]. Taken together our data indicate that PatJ regulates the apical actin cytoskeleton to control the delivery of apical cargo to the AMIS, leading to correct lumen initiation and the formation of a microvilli rich apical cell surface.

Discussion

Here we used time-resolved proximity proteomics, super-resolution imaging, and electron microscopy to dissect the molecular and ultrastructural events that orchestrate the establishment of epithelial cell polarity. We present a temporally resolved protein interaction network that provides a rich resource for dissecting the molecular basis of epithelial cell junction assembly and polarity development. We also identified VACs as important transport carriers for apical lumen initiation and show that Pals1 and PatJ are critical for the delivery of VACs to the prospective apical luminal domain. Our work redefines the mechanisms of *de novo* lumen formation in MDCK 3D cultures, with potentially broad implications for lumenogenesis in other cell types and tissues.

Time-resolved spatial proteomics defines a dynamic protein network during cell-cell junction assembly

We employed a combination of APEX2-TEM labeling and temporally controlled proximity proteomics to resolve distinct stages of cell-cell junction assembly and polarity development using the calcium switch assay. Altogether the data indicate that apical cargo is delivered to nascent cell contacts via VACs. VAC exocytosis is temporally coordinated with the assembly of cell-cell junctions and is followed by the formation of a microvilli-rich lumen at the lateral domain. Our proteomics data shows that the integral TJ membrane proteins JAM-A (F11R), claudin-1 and claudin-4 become enriched at nascent cell contacts at a time when VAC exocytosis is most prominent (0.5-2h). By contrast, all TJ scaffolding proteins including ZO-1, ZO-3, CGN, and Par3 were recruited later (2-6h). This indicates that the coalescence of TJ membrane proteins precedes the recruitment of TJ scaffolding proteins, which agrees with the role of claudins as ZO receptors and with data showing that JAM-A is one of

the first adhesion molecules to appear at sites of cell-cell contact formation and recruits ZO-1 and Par3 to initiate TJ assembly [56,57]. Interestingly, the GTPases RalA was recruited together with JAM-A. RalA is required for TJ formation and regulates the activity of the exocyst complex [58]. Given that the exocyst complex interacts with Par3 to mediate the fusion of exocytic cargo at the lateral cortex [59-61], it is tempting to speculate that Par3, RalA and the exocyst are involved in the exocytosis of VACs at nascent cell contacts.

Our proteomics data also revealed intriguing new insights into the kinetics of Rho and Ras GTPases during cell junction assembly. Whilst the RhoGTPases Cdc42, Rac1 and RhoA/C and several actin assembly factors became transiently enriched at early stages of junction assembly (0.5h), RasGTPases such as Rap1A, KRas and NRas peaked later together with JAM-A (2h) and remained associated with cell junctions until they had fully matured. These temporal recruitment profiles are in agreement with the reported functions of Rho/Ras GTPases at cell-cell junctions [62-66]. For instance, Cdc42 regulates membrane trafficking and the recruitment of the Par complex to nascent cell junctions to establish cell polarity [67]. Rac promotes the polymerization of branched actin networks at primordial cell contacts, whilst RhoA-mediated contractility is required at later stages for junction reinforcement and expansion [68,69]. Interestingly, and consistent with the late recruitment of Rap1A observed in our proteomics data, Rap1 was shown to suppress RhoA activity at endothelial cell junctions, possibly via the activation of Cdc42 [70,71]. Similarly, Rap2C was recruited at late stages of junction assembly and has been implicated in the control of a functional TJ barrier downstream of JAM-A and ZO-2 [72]. Altogether the data indicate that the assembly and maturation of the AJC is accompanied by a switch from RhoGTPase-based to Ras-mediated signaling.

VMZ and TJ scaffolding proteins as well as components of the junction-associated actin cortex became progressively enriched with Pals1, reaching a plateau at late stages of junction assembly (4-6h). This suggests that junctional proteins coalesce (i.e. become gradually concentrated) at the membrane as the AJC is formed. This is consistent with the concept that TJ assembly is driven by phase separation of ZO-1 scaffolds and the junctional actin cytoskeleton [73,74]. Interestingly, PatJ was recently shown to promote the spreading of ZO-1 condensates along the apical-lateral interface, possibly by providing a physical link between the ZO scaffold and the apical Crumbs complex [38]. Our TEM data supports this model in demonstrating that Pals1 localises apical of TJs as soon as the AJC is formed and apico-basal polarity is established. Our data and that of others also clearly show that PatJ and Pals1 are critical for the assembly of a functional TJ barrier [33,34,38,40], suggesting that the VMZ plays an important role in shaping and functionalizing the apical-lateral border.

VACs act as intracellular precursors for apical domain initiation

We show here that VACs are a characteristic feature of MDCK cells grown in Matrigel. The data suggest that VACs arise through the internalization of microvilli-enriched membrane pits from the ECM-facing plasma membrane. How apical proteins are concentrated in such pits and internalized is currently unclear but could involve Rho/ROCK signaling downstream of integrin adhesions [75]. VACs are then transported to the AMIS and fuse with the local membrane to establish the site of the future lumen. Again, the mechanisms underlying VAC transport and fusion at the AMIS remain to be determined, yet microtubule-based transport [21] and the exocyst complex [16] may be involved. Since VACs are large vacuoles that contain a pre-assembled apical cortex,

we propose that bulk exocytosis of VACs at the AMIS permits rapid and efficient initiation of apical domain identity.

VACs were originally identified in calcium-depleted MDCK cells [43,44]. Similar structures were then observed in various cell types grown under normal conditions [76-78], demonstrating that VACs are not an artifact of calcium depletion. More recently, VAC-like structures have been observed in stem cells (SCs) and tissues. For instance, isolated human embryonic SCs express a perinuclear compartment dubbed "apicosome" [17,79]. Apicosomes contain microvilli and apical proteins (such as atypical PKC and PODXL), are enriched in calcium, and have been shown to mediate apical lumen initiation and expansion in human and mouse blastocysts [12,13] and in a human pluripotent SC-derived epiblast model [80]. Large intracellular organelles containing apical markers have also been described during lumen formation in the mouse axial mesoderm [81]. Moreover, intracellular VAC-like structures were observed in response to loss of Cdc42 in the mouse pancreas [82] and in microvillus inclusion disease, which is caused by mutations in the apical motor protein MYO5B [83]. Interestingly, in the *Drosophila* midgut pre-enterocytes establish an apical pole way before they are incorporated into the intestinal epithelium [84,85]. This so-called preassembled apical compartment (PAC) is an apical cavity circumscribed by cell-cell junctions with adjacent enterocytes, making it somewhat similar to the apical luminal surface formed in the calcium switch assay. This data together with the work presented here indicates that VAC-like compartments represent a common and evolutionarily conserved organelle required for apical membrane assembly.

Current models of *de novo* lumen formation in MDCK cells posit that apical cargo (such as the commonly used PODXL protein) is delivered to the AMIS via vesicular transport. Such carriers contain apical Rab proteins including Rab3, Rab8 and Rab11 and are proposed to be of recycling endosomal nature [2-4,16]. However, our data and careful examination of the MDCK cell literature indicates that PODXL-containing transport carriers do not always appear vesicular. In fact, Crb3 [36], Rab11 [19], IRSp53 [25], Rab35 [24], and the synaptotagmin-like protein Slp2 [22] (to name a few) often colocalise with PODXL in large intracellular vacuoles highly reminiscent of VACs. In addition, apical cargo frequently accumulates in such vacuoles upon perturbation of the apical trafficking machinery, TJ proteins, or polarity factors [19,21,22,24,25,36,75,86]. This indicates that VACs have been observed previously but were not reported as such. It is evident that VACs can only be effectively resolved using TEM or state-of-the-art super resolution microscopy. However, to our knowledge only two studies have analysed the ultrastructure of early stage MDCK cell cysts [25,87], and these studies only examined small volumes of the entire cell doublet, possibly explaining why VAC-like structures were not reported before. Altogether, we propose that VACs are distinct intracellular apical precursors that function in parallel with the vesicular transport machinery to deliver apical cargo to the AMIS.

Our TEM analysis revealed remarkable similarities between VAC exocytosis in the calcium switch assay and that observed at the AMIS in 3D cultures. In both systems sites of VAC fusion and nascent luminal surfaces were surrounded by a junctional belt. This indicates that the exocytosis of VACs is temporally coordinated with the formation of cell-cell junctions. In case of the calcium switch assay, the data imply that the microvilli-rich lumen that is formed at the lateral membrane needs to move apically to generate a free apical surface (Figure 2F). Interestingly, loss of Par3 has been shown to cause an arrest of VACs at the lateral membrane [86] and a similar phenotype can be evoked by overexpression of Par1 [88]. This suggests that the Par polarity proteins are involved in redirecting the nascent lateral lumen to the apical

surface. In case of the 3D system, our data suggest that the AJC is assembled concomitantly with the arrival of VACs at the AMIS (Figure 6). This raises several questions: 1) What triggers the clearance of lateral adhesions at the AMIS to allow the AJC to be assembled? 2) How do E-Cadherin based adhesions and TJ proteins establish their apico-basal orientation during the AMIS/PAP transition? And 3) how are VAC fusion and junction assembly coordinated? Answering these questions will be critical to fully decipher the mechanisms underlying *de novo* apical domain assembly.

Role of Pals1 and PatJ in lumen initiation

Based on transfection experiments with GFP-tagged proteins it was proposed that Crb3 is transported together with Pals1 and PatJ to the AMIS via Rab11-positive transport carriers [36]. Our localization studies using antibodies against the endogenous proteins do not support this model. Instead, we find that Pals1 and PatJ localize to cell-cell contacts and the AMIS before apical cargo (PODXL and ezrin) arrives. Although the lack of a suitable antibody prevented us from examining the localization of endogenous Crb3 during lumen initiation, others have shown that Crb3 and PODXL are transported to the AMIS in a common transport carrier [24,36]. The combined data suggest that the full Crumbs complex is not assembled until Crb3 is delivered to the AMIS.

We further show that 3D lumenogenesis and the delivery of VACs to the AMIS are severely compromised in cells lacking PatJ or Pals1. This suggests that PatJ/Pals1 are required for the fusion of VACs at the AMIS and thereby mediate the delivery of Crb3 and other important lumen forming factors (such as PODXL) to the nascent apical cortex. Indeed, Pals1 forms a high affinity complex with the Crb3 C-terminal tail [89], suggesting that Pals1 may act as the VAC cargo receptor. Interestingly, suppression of Rho/ROCK signaling or myosin-II activity in MDCK WT cells was sufficient to perturb VAC exocytosis at the AMIS. In addition, loss of PatJ resulted in a marked reduction in apical F-actin levels and a disorganization of the apical cortex. Together with the observation that junctional RhoA levels are reduced in Pals1 KO MDCK cells [40], this suggests that PatJ/Pals1 control apical lumen initiation by promoting Rho-mediated F-actin assembly and contractility at the apical-lateral interface. Several reports have indeed demonstrated that the actin cytoskeleton plays a critical role during lumen initiation [4,21,87,90] and that the Crumbs complex controls apical actomyosin contractility via ROCK [51,52] and ArhGEF18 (p114RhoGEF; Cysts in *Drosophila*) [49,50,53,54,91]. Since PatJ interacts directly or indirectly with several actin regulators including ArhGEF18, Homer proteins, PKN2 and ArhGAP29 [39,42], it is possible that PatJ serves as a cortical scaffold for the regulation of the actin cytoskeleton at the apical-lateral border. Future work should test this idea and address the mechanistic basis of how the Crumbs complex controls the assembly, structure and function of the apical luminal surface.

Acknowledgements

We thank Hi-Tech Instruments Pte Ltd and Hitachi High-Tech Corporation for the FIB-SEM analysis and Thomas Weide for providing Pals1 KO cells. This work was supported by a Singapore Ministry of Education (MOE) Academic Research grant Tier2 (MOE-T2EP30121-0019) to A.L. E.M. was supported by an FNR AFR Bilateral Singapore grant (11823257) to G.D. and A.L.

Author contributions

E.M. performed Pals1-A2E and Rab experiments, generated samples for proteomics, and analysed the proteomics data, S.G. performed MDCK 3D cyst experiments, Y.C.

generated PatJ KO cells, R.G. acquired MS data, B.H. performed parts of the TEM analysis, K.E.L. performed the SEM analysis and prepared samples for FIB-SEM, G.D. supervised E.M. and R.G. during the early stages of the project and overlooked the proteomics analysis, A.L. supervised E.M., S.G., Y.C., R.G. and B.H., conceived the project, performed TEM analysis, and wrote the manuscript.

Declaration of conflict of interest
The authors declare no conflict of interest

Materials and Methods

DNA constructs
The Pals1-A2E MDCK-II cell line was described previously [39]. C1-EGFP-hPMCA2w/b (plasmid #47586), C1-EGFP-Rab3a (plasmid #49542, GenBank: AF498931) and C1-EGFP-Rab35 (plasmid #49552, GenBank: NM_006861) were purchased from Addgene. C1-EGFP-Rab1a (GenBank: NM_00416) and C1-EGFP-Rab6a (GenBank: NM_198896) were provided by Lu Lei. C1-EGFP-Rab11a (GenBank: NM_001003276) was provided by Ben Nichols. The cDNA for Rab25 (GenBank: BC033322, IMAGE clone: 4775725) was provided by the Protein Production Platform, Nanyang Technological University. To produce APEX2-EGFP versions of Rab1a, Rab3a, Rab6a, Rab11a, Rab25 and Rab35, the cDNAs were cloned into the C1-A2E vector [39] using FastCloning. pX458 (Addgene plasmid #48138) was provided by Francesc Xavier Roca Castella. Single guide RNA sequences were inserted using the *BbsI* site. All constructs were verified by Sanger sequencing.

Cell culture
MDCK-II cells were cultured in high glucose DMEM with pyruvate and GlutaMAX™ supplement (Gibco, 10569010) supplemented with 10 % FBS, 100 units/mL penicillin, and 100 µg/mL streptomycin at 37 °C and 5 % CO_2. Cells were allowed to grow to confluence before passaging. Trypsinisation was performed by washing with Phosphate Buffered Saline (PBS) pH 7.4 (Gibco) followed by incubation with 0.25% trypsin-EDTA (Gibco) until detached. For monolayers requiring complete polarisation, MDCK-II cells were seeded into 0.4 µm-pore Transwell® filter inserts (Corning) at an initial density of ~2 x 10^5 cells/cm^2. Media was changed every two days by aspirating out old media and adding in fresh media. Cells were grown on the filter inserts for 10-14 days to achieve full polarisation.

Generation of stable cell lines and CRISPR/Cas9 knockout lines
Cells were transfected with Lipofectamine 3000 (Invitrogen) according to the manufacturer's instructions. For the generation of stable cell lines expressing APEX2-EGFP fusion constructs, MDCK-II cells were selected with 500 µg/mL geneticin (GIBCO) for at least 14 days post-transfection and subsequently FACS sorted for GFP positive cells. Pals1 MDCK KO cells have been described previously [40]. For the generation of CRISPR/Cas9 PatJ knockout cells, three sgRNAs (see Supplemental Table 1) were designed from the Benchling App, each targeting specific 20 nt-long sequences in early exons (exon 4, 11, 16) of the canine *PatJ* gene. These gene locations correspond to the L27 (sgRNA2), PDZ3 (sgRNA1), and PDZ4 (sgRNA3) domains of PATJ, respectively. The sgRNAs were inserted into the pX459 backbone, which also encodes the tracrRNA scaffold and Cas9 protein, and transfected into

MDCK-II cells. MDCK-II cells were co-transfected with C1-EGFP and two pX459 sgRNA plasmids in a 1:4 ratio. Cells were selected with 500 µg/mL geneticin (Gibco) for at least 14 days post-transfection. The cells were then GFP FACS sorted as single cells into 96 well plates. Single cell clones were expanded and screened by Western blotting. Three PatJ KO lines (E4, E6, E8) were selected from cells co-transfected with sgRNA1 and sgRNA3. Their genomic DNA was extracted to amplify the sgRNA1 (exon 11) target site by PCR. The purified PCR products were submitted for DNA sequencing. The three KO lines were genetically identical, having a 247 bp insertion in exon 11, resulting in a premature stop codon in the PDZ3 domain.

MDCK 3D cultures

For 3D cyst assays, MDCK-II cells were split sparsely (~1:10-1:50) to obtain sub-confluent cell cultures. Matrigel® (Corning) of the required quantity was left at 4°C to thaw overnight. All steps using Matrigel® were performed on ice unless otherwise stated. The following day, glass-bottomed 8-well chamber slides (IBIDI) were coated with ~4 µL Matrigel® per well and left undisturbed in the 37°C incubator to polymerise for 30-45 mins. In the meantime, MDCK-II cells were trypsinised and counted. Single cells were resuspended in 200 µL/well of 2% Matrigel® and seeded at a density of 30,000-50,000 cells/well. The 2% Matrigel® media was replenished every two days. Cysts were cultured for 16-20 h for the inverted polarity and AMIS stages, 20-24 h for the PAP and early lumen stages, and up to 4 days for the mature end-stage of lumen formation.

Calcium switch assay

Low calcium media was formulated using DMEM without calcium chloride (Gibco, 21068028) supplemented with 3 µM calcium chloride, 110 mg/L (1 mM) sodium pyruvate, 3.97 mM L-alanyl-glutamine (GlutaMAX™), 100 units/mL penicillin, 100 µg/mL streptomycin, and 5 % dialysed FBS. Normal calcium media was prepared by supplementing low calcium media with 1.8 mM $CaCl_2$. MDCK-II cells were seeded at 50% density and grown to confluence overnight in 24-well plates on glass coverslips. Cells were washed twice with PBS and subsequently incubated in low calcium media overnight (16-24h) for complete disassembly of cell junctions. Media was then replaced with normal calcium media and cells were fixed and analysed at defined time points post-calcium addition.

Immunofluorescence microscopy

MDCK monolayers and MDCK cells grown in Matrigel were washed thrice with PBS pH 7.4 followed by fixation with 1% paraformaldehyde (PFA) in PBS pH 7.4. Monolayers were fixed for 20 min at room temperature, whilst 3D cysts were fixed for 30 min at room temperature. 3D cysts were permeabilised in PBS pH 7.4 containing 0.2% Triton X-100 for 20 min, while monolayers were permeabilised in PBS 0.5% Triton X-100 for 15 min and washed thrice again with PBS. Samples were blocked with 10% FBS in 0.2 µm-filtered PBS pH 7.4 for at least 2 h at room temperature or overnight at 4°C, and then incubated with primary antibodies diluted in antibody incubation buffer (0.2 µm-filtered PBS pH 7.4, 0.1% BSA, 0.01% Tween-20) for 1-3 h at room temperature or overnight at 4°C. Samples were washed three times for 5 min each in antibody incubation buffer and further incubated for 1 h with fluorescently conjugated secondary antibody diluted in antibody incubation buffer at room temperature in the dark (see Supplemental Table 1 for all antibodies used). Samples were again washed thrice for 10 min each in PBS and stained for 10 min with 20 ng/mL

DAPI (Sigma) diluted in PBS. For cells grown on Transwell® filter inserts (Corning), filter inserts were cut out with a sharp razor blade post blocking. For staining and washes, filter pieces were laid face-up on a piece of parafilm in a humidified chamber and overlaid with ~25 µl of staining/wash solution. Glass coverslips were laid face-down over ~40 µl of staining solutions on parafilm in a humidified chamber and were laid face-up on parafilm for washes. Filter pieces were placed face-up on glass slides, overlaid with mounting medium and covered with #1.5 (12 mm) glass coverslips (VWR). Cells were stained with DAPI (1 ug/mL in PBS) prior to mounting in mounting medium (Vectashield, Vector Laboratories H-1000). Coverslips were sealed with transparent nail polish and stored at 4°C. Monolayers grown on glass bottom dishes or Transwell® filters were imaged using the CorrSight spinning disk confocal microscope (ThermoScientific) equipped with an Orca R2 CCD camera (Hamamatsu) using a 40x oil objective (NA 1.3, Zeiss) or a 63x oil objective (NA 1.4, Plan Apochromat M27, Zeiss) and standard filter sets. Most 3D cyst samples were imaged with the Airyscan confocal systems LSM710, 880 or 980 (Zeiss) using a 100x oil objective (Zeiss, NA 1.46). 3D Structured Illumination Microscopy (3D-SIM) was performed on a Zeiss Elyra 7 with Lattice SIM. Confocal images were processed in Zeiss Zen software and ImageJ/FIJI [92,93].

Live cell imaging

MDCK-II cells stably expressing Pals1-A2E were grown on glass-bottom dishes (MatTec Corp., Ashland, MA) and imaged live in low calcium media with a CorrSight spinning disk microscope (Thermo Fisher Scientific). Imaging was carried out at 37 °C, 5 % CO_2 and 90 % humidity in a closed atmosphere chamber (IBIDI). 8 different locations were imaged simultaneously using the multi-stage position function in LA software (Thermo Fisher Scientific) and confocal images were acquired using a 63x oil objective (Plan Apochromat M27, Zeiss, NA 1.4) and the 488 nm laser line (65 mW; iChrome MLE-LFA) and a standard GFP filter set. Focus was maintained by a hardware autofocus system (Focus Clamp). The laser output power and exposure times were set to a minimum.

Antibody internalisation assay

MDCK-II cysts were cultured in Matrigel®. At 16 h, Podocalyxin antibody and/or Wheat Germ Agglutinin (WGA) (Biotium, CF®633 WGA 29024-1) were added to the media and incubated for at least 2 hours before washing off. The cysts were then fixed at 2 h intervals between the 18 to 24 h time points, permeabilised, blocked, stained with Phalloidin and secondary antibody, and imaged using an Airyscan LSM980 confocal microscope (Zeiss) using a 100x oil objective (Zeiss, NA 1.46).

Transmission electron microscopy

MDCK-II cells grown on glass bottom dishes (MatTec Corp., Ashland, MA) or in Matrigel were fixed with 2% glutaraldehyde (EMS) in 0.1 M cacodylate buffer (CB) (sodium cacodylate pH 7.4, 2 mM $CaCl_2$) at room temperature for 5 min followed by incubation on ice for 1-2h. APEX2 labeling was performed as previously described [39,45,94]. Cells were post-fixed with 1% osmium tetroxide (OsO_4) (EMS) in CB containing 1% potassium ferricyanide ($K_3[Fe(CN)_6]$) (EMS). For TEM of 3D cysts, lateral membrane contrast was enhanced through incubation with 1% low molecular weight tannic acid $(C_{14}H_{10}O_9)_n$, (EMS) in CB for 1 h at room temperature. In some instances, samples were *en bloc* stained with 1% uranyl acetate (UA) (EMS) in ultrapure water overnight at 4°C. Samples were dehydrated in a cold graded ethanol series (20%,

50%, 70%, 90%, 100%) for 2-5 min each, followed by two washes in 100% anhydrous ethanol (EMS) for 3 min each. Samples were then infiltrated with a Durcupan resin:ethanol gradient (1:2, 1:1, 2:1) for 45 min each followed by infiltration in 100% resin overnight. Five to eight more resin exchanges were performed for 45 min each at 45°C. Resin-embedded samples were polymerised at 60°C for 2 days. Samples were sectioned into 70-80 nm thick sections and mounted onto formvar and carbon-coated slot grids (EMS). Transmission electron microscopy (TEM) was performed using a Tecnai T12 TEM (FEI) operated at 120 kV. Electron micrographs were captured using a 4k x 4k Eagle CCD camera (FEI) and processed in ImageJ/FIJI.

Focused Ion Beam (FIB)-SEM

For FIB-SEM, MDCK-II cells embedded in Matrigel for 24h were chemically fixed and processed following the osmium-thiocarbohydrazide-osmium (OTO) method, along with *en bloc* UA and lead aspartate staining before being embedded in resin [95]. The specimen was trimmed into blocks less than 1000 μm^3 in volume, mounted on aluminium pins, sputter-coated with platinum (LEICA EM ACE200), and imaged on a Hitachi NX9000 FIB-SEM. FIB slicing was performed at 30 kV acceleration voltage using a probe current of 12 nA and a slicing pitch/step size of 30 nm. The block face was imaged at 2 kV acceleration voltage using the BSE detector and an exposure time of 100 sec. The recorded images had a voxel size of 10 nm (x) x 10 nm (y) x 30 nm (z). FIB-SEM data was further processed in ImageJ/FIJI.

Scanning Electron Microscopy

MDCK-II cells grown on Transwell filters for 16 days were fixed with 2% glutaraldehyde (EMS) and 2% EM grade paraformaldehyde (EMS) in 0.1 M cacodylate buffer (CB) (sodium cacodylate pH 7.4, 2 mM $CaCl_2$) at room temperature for 5 min followed by incubation at 4°C for 2h. The samples were post-fixed with 1% OsO_4 for 1 hour, dehydrated in a graded ethanol series (25%, 50%, 75%, 90% and 100%), dried using a critical point drier (LEICA EM CPD300), sputter coated with gold (LEICA EM ACE200), and examined at 5 kV using a Scanning Electron Microscope (Quanta 650FEG, FEI).

Proximity biotinylation

APEX2 proximity biotinylation was carried out as described previously [39,46]. Briefly, MDCK-II cells stably expressing Pals1-A2E were incubated in media containing 2.5 mM biotin phenol (Iris Biotech) for 30 minutes at 37 °C. Cells were washed twice with PBS and the APEX reaction was initiated by incubating with 250 mM H_2O_2 for 1 minute at room temperature. The APEX2 reaction was quenched by washing three times with the quencher solution (PBS containing 5 mM (±)-6-hydroxy-2,5,7,8-tetramethylchromane-2 carboxylic acid (Trolox), 10 mM sodium ascorbate, 10 mM sodium azide) prior to lysis in ice-cold lysis buffer (1 % sodium deoxycholate in 50 mM ammonium bicarbonate pH 8.0).

Streptavidin purification and on-bead digestion

Lysates were sonicated briefly (2 x 20 second cycles) and clarified through centrifugation at 20,000 xg for 30 min at 4 °C. Protein concentrations were measured by Bradford and equalized. High-capacity streptavidin sepharose beads (GE healthcare) were washed once with 40 % methanol and twice with ice-cold lysis buffer (1 % sodium deoxycholate in 50 mM ammonium bicarbonate pH 8.0) prior to incubation with protein lysates (50 µL bead slurry per 3 mg total protein) for 2 h at 4

°C on a rotator. Beads were then washed twice with cold lysis buffer, and then once with each of the following washing buffers: 1 M KCl, 0.1 M Na_2CO_3, 2 M Urea in 50 mM ammonium bicarbonate pH 8.0. The last two washes were performed with cold 50 mM ammonium bicarbonate pH 8.0. Beads were then re-suspended in 2 M Urea in 50 mM ammonium bicarbonate pH 8.0 and protein reduction was performed by incubating with DTT at a final concentration of 10 mM for 45 min at 37 °C and 800 rpm. Samples were subsequently alkylated through incubation with iodoacetamide at a final concentration of 25 mM for 30 min at room temperature and 800 rpm. Samples were pre-digested with 0.5 µg LysC for 4 h at 37 °C and 800 rpm and then digested with 1 µg trypsin overnight at 37 °C and 800 rpm. Peptides were acidified to pH 2 by adding formic acid to 1 % final concentration and centrifuged for 15 min at 16,000 rpm at 4 °C to remove any precipitates or beads on Sep-Pak µ-C18 Elution Plates. Peptides were then dried on a speed vac for 2 hours and re-suspended in 0.1% formic acid prior to LC-MS.

Mass spectrometry

LC-MS/MS was performed using an Ultimate 3000 RSLCnano (Thermo Fisher Scientific) LC system equipped with an Acclaim PepMap RSLC column (15 cm × 75 µm, C18, 2 µm, 100 Å, Thermo Fisher Scientific). Peptides were eluted at a flow rate of 300 nL/min in a linear gradient of 2-35% solvent B over 70 minutes (solvent A: 0.1% formic acid; B: 0.1% formic acid in acetonitrile (ACN)), followed by a 5 minutes washing step (90% solvent B) and a 10 minutes equilibration step (2% solvent B). Mass spectrometry was performed on a Q-Exactive Plus mass spectrometer (Thermo Fisher Scientific) equipped with a nano-electrospray source and using uncoated SilicaTips (12 cm, 360 µm o.d., 20 µm i.d., 10 µm tip i.d.) for ionization, applying a 1500 V liquid junction voltage at 250°C capillary temperature. MS/MS analysis were performed in data dependent acquisition (DDA) mode, and the 12 most intense parent ions were fragmented with a resolving power of 17500 (at 200 m/z). Automatic gain control (AGC), maximum fill time and dynamic exclusion were set to $1e^6$, 60 ms and 30 ms respectively.

Mass spectrometry and data processing

LC-MS/MS was performed using an Ultimate 3000 RSLCnano (Thermo Fisher Scientific) LC system equipped with an Acclaim PepMap RSLC column (15 cm × 75 µm, C18, 2 µm, 100 Å, Thermo Fisher Scientific). Peptides were eluted at a flow rate of 300 nL/min in a linear gradient of 2-35% solvent B over 70 minutes (solvent A: 0.1% formic acid; B: 0.1% formic acid in acetonitrile (ACN)), followed by a 5 minutes washing step (90% solvent B) and a 10 minutes equilibration step (2% solvent B). Mass spectrometry was performed on a Q-Exactive Plus mass spectrometer (Thermo Fisher Scientific) equipped with a nano-electrospray source and using uncoated SilicaTips (12 cm, 360 µm o.d., 20 µm i.d., 10 µm tip i.d.) for ionization, applying a 1500 V liquid junction voltage at 250°C capillary temperature. MS/MS analysis were performed in data dependent acquisition (DDA) mode, and the 12 most intense parent ions were fragmented with a resolving power of 17500 (at 200 m/z). Automatic gain control (AGC), maximum fill time and dynamic exclusion were set to $1e^6$, 60 ms and 30 ms respectively.

Analysis of time-resolved proteomes

Protein quantification was performed with MaxQuant (version 1.6.17.0) using the following parameters: carbamidomethyl cysteine as fixed modification, methionine

oxidation and N-acetylation as variable modifications, digestion mode trypsin specific with maximum 2 missed cleavages, and an initial mass tolerance of 4.5 ppm for precursor ions and 0.5 Da for fragment ions. All experiments were performed in quadruplicate except for the no peroxide sample which was performed in triplicate. The abundance of assembled proteins was determined using label-free quantification with the match between runs option was selected. Protein identification was performed searching against the Uniprot reference proteome (Uniprot ID 9615, downloaded on 06 January 2020). Proteins tagged as “Potential contaminants”, “Reverse”, and “Only identified by site” were removed from the analysis. Proteins were matched with their respective human gene names as described in Tan et. al., [39]. A moderated T-test was performed using the Proteomics Toolset for Integrative Data Analysis (ProTIGY, Broad Institute, Proteomics Platform, https://github.com/broadinstitute/protigy). Data was filtered to include only proteins with a minimum of two replicate identifications at each timepoint across the timecourse dataset. Proteins which were found to be significantly enriched with a p-value less than 0.05 and a log2 fold change greater than 1.0 as compared to both controls were considered for further analysis. 20 proteins (CGN, IRF3, ISG15, KRAS, LGALS9, LMO7, MYO1B, PARD3, PKN2, PPP1R9A, PSME3, PTPN13, RAB35, RPL19, SCRN3, SLC25A1, SLC25A6, TJP1, USP6NL, WASL) which were not found to be significantly enriched, but were identified in our previously published Pals1 proximity proteome [39] and satisfied all other criteria were also considered for further analysis. The final proximity proteome encompassed 278 proteins (see Supplemental File 1). Further data analysis and visualization were performed in R (version 4.1.2). Data clustering and heatmap generation were carried out using the ComplexHeatmap package in R. Enrichment analysis was carried out using the Enrichr analysis tool (https://maayanlab.cloud/Enrichr/).

Generation of interactome

Interaction entries were retrieved from the BioGRID (version 4.3.195) and STRING databases. For BioGRID entries, only physical protein interactions were considered. For STRING entries, only experimental and database interactions with a combined confidence score > 0.4 were included.

Quantifications and statistical analyses

Immunofluorescence images were processed and analysed on Zeiss Zen (particularly for Airyscan images) or ImageJ/FIJI software [92,93]. Line scans were performed by drawing lines of similar lengths across junctions and comparing the RGB plot profiles of the different channels. Pearson’s correlation coefficients were obtained using the Coloc2 plugin in ImageJ by marking the junctions as regions of interest. For other values like length, area etc the suitable Measure functions of ImageJ were used. For the measurement of apical F-actin intensity, cell boundaries were segmented using Cellpose [96] and apical F-actin intensity measured using maximum intensity projections of the apical portion of the z-stack. Statistical analysis was performed using two-tailed unpaired student t-test analysis on GraphPad Prism. All data represent at least three independent repeats: n.s, not significant, *$p<0.05$, **$p<0.01$, ***$p<0.001$, ****$p<0.0001$, unless stated otherwise. Values are represented in mean ± SEM unless stated otherwise.

References

1. Datta, A., Bryant, D.M., and Mostov, K.E. (2011). Molecular regulation of lumen morphogenesis. Curr Biol *21*, R126-136. 10.1016/j.cub.2010.12.003.
2. Apodaca, G., Gallo, L.I., and Bryant, D.M. (2012). Role of membrane traffic in the generation of epithelial cell asymmetry. Nature cell biology *14*, 1235-1243. 10.1038/ncb2635.
3. Blasky, A.J., Mangan, A., and Prekeris, R. (2015). Polarized protein transport and lumen formation during epithelial tissue morphogenesis. Annu Rev Cell Dev Biol *31*, 575-591. 10.1146/annurev-cellbio-100814-125323.
4. Jewett, C.E., and Prekeris, R. (2018). Insane in the apical membrane: Trafficking events mediating apicobasal epithelial polarity during tube morphogenesis. Traffic. 10.1111/tra.12579.
5. Roman-Fernandez, A., and Bryant, D.M. (2016). Complex Polarity: Building Multicellular Tissues Through Apical Membrane Traffic. Traffic *17*, 1244-1261. 10.1111/tra.12417.
6. Sigurbjornsdottir, S., Mathew, R., and Leptin, M. (2014). Molecular mechanisms of de novo lumen formation. Nat Rev Mol Cell Biol *15*, 665-676. 10.1038/nrm3871.
7. Marciano, D.K. (2017). A holey pursuit: lumen formation in the developing kidney. Pediatric nephrology *32*, 7-20. 10.1007/s00467-016-3326-4.
8. Yang, Z., Zimmerman, S., Brakeman, P.R., Beaudoin, G.M., 3rd, Reichardt, L.F., and Marciano, D.K. (2013). De novo lumen formation and elongation in the developing nephron: a central role for afadin in apical polarity. Development *140*, 1774-1784. 10.1242/dev.087957.
9. Gerlach, G.F., and Wingert, R.A. (2014). Zebrafish pronephros tubulogenesis and epithelial identity maintenance are reliant on the polarity proteins Prkc iota and zeta. Dev Biol *396*, 183-200. 10.1016/j.ydbio.2014.08.038.
10. Bagnat, M., Cheung, I.D., Mostov, K.E., and Stainier, D.Y. (2007). Genetic control of single lumen formation in the zebrafish gut. Nature cell biology *9*, 954-960. 10.1038/ncb1621.
11. Alvers, A.L., Ryan, S., Scherz, P.J., Huisken, J., and Bagnat, M. (2014). Single continuous lumen formation in the zebrafish gut is mediated by smoothened-dependent tissue remodeling. Development *141*, 1110-1119. 10.1242/dev.100313.
12. Ryan, A.Q., Chan, C.J., Graner, F., and Hiiragi, T. (2019). Lumen Expansion Facilitates Epiblast-Primitive Endoderm Fate Specification during Mouse Blastocyst Formation. Dev Cell *51*, 684-697 e684. 10.1016/j.devcel.2019.10.011.
13. Bedzhov, I., and Zernicka-Goetz, M. (2014). Self-organizing properties of mouse pluripotent cells initiate morphogenesis upon implantation. Cell *156*, 1032-1044. 10.1016/j.cell.2014.01.023.
14. Shahbazi, M.N., Jedrusik, A., Vuoristo, S., Recher, G., Hupalowska, A., Bolton, V., Fogarty, N.N.M., Campbell, A., Devito, L., Ilic, D., et al. (2016). Self-organization of the human embryo in the absence of maternal tissues. Nature cell biology *18*, 700-708. 10.1038/ncb3347.
15. Martin-Belmonte, F., Yu, W., Rodriguez-Fraticelli, A.E., Ewald, A.J., Werb, Z., Alonso, M.A., and Mostov, K. (2008). Cell-polarity dynamics controls the mechanism of lumen formation in epithelial morphogenesis. Curr Biol *18*, 507-513. 10.1016/j.cub.2008.02.076.
16. Bryant, D.M., Datta, A., Rodriguez-Fraticelli, A.E., Peranen, J., Martin-Belmonte, F., and Mostov, K.E. (2010). A molecular network for de novo

generation of the apical surface and lumen. Nature cell biology *12*, 1035-1045. 10.1038/ncb2106.
17. Taniguchi, K., Shao, Y., Townshend, R.F., Tsai, Y.H., DeLong, C.J., Lopez, S.A., Gayen, S., Freddo, A.M., Chue, D.J., Thomas, D.J., et al. (2015). Lumen Formation Is an Intrinsic Property of Isolated Human Pluripotent Stem Cells. Stem cell reports *5*, 954-962. 10.1016/j.stemcr.2015.10.015.
18. Strilic, B., Kucera, T., Eglinger, J., Hughes, M.R., McNagny, K.M., Tsukita, S., Dejana, E., Ferrara, N., and Lammert, E. (2009). The molecular basis of vascular lumen formation in the developing mouse aorta. Dev Cell *17*, 505-515. 10.1016/j.devcel.2009.08.011.
19. Roman-Fernandez, A., Roignot, J., Sandilands, E., Nacke, M., Mansour, M.A., McGarry, L., Shanks, E., Mostov, K.E., and Bryant, D.M. (2018). The phospholipid PI(3,4)P2 is an apical identity determinant. Nat Commun *9*, 5041. 10.1038/s41467-018-07464-8.
20. Martin-Belmonte, F., Gassama, A., Datta, A., Yu, W., Rescher, U., Gerke, V., and Mostov, K. (2007). PTEN-mediated apical segregation of phosphoinositides controls epithelial morphogenesis through Cdc42. Cell *128*, 383-397. 10.1016/j.cell.2006.11.051.
21. Mangan, A.J., Sietsema, D.V., Li, D., Moore, J.K., Citi, S., and Prekeris, R. (2016). Cingulin and actin mediate midbody-dependent apical lumen formation during polarization of epithelial cells. Nat Commun *7*, 12426. 10.1038/ncomms12426.
22. Galvez-Santisteban, M., Rodriguez-Fraticelli, A.E., Bryant, D.M., Vergarajauregui, S., Yasuda, T., Banon-Rodriguez, I., Bernascone, I., Datta, A., Spivak, N., Young, K., et al. (2012). Synaptotagmin-like proteins control the formation of a single apical membrane domain in epithelial cells. Nature cell biology *14*, 838-849. 10.1038/ncb2541.
23. Elias, B.C., Das, A., Parekh, D.V., Mernaugh, G., Adams, R., Yang, Z., Brakebusch, C., Pozzi, A., Marciano, D.K., Carroll, T.J., and Zent, R. (2015). Cdc42 regulates epithelial cell polarity and cytoskeletal function during kidney tubule development. Journal of cell science *128*, 4293-4305. 10.1242/jcs.164509.
24. Klinkert, K., Rocancourt, M., Houdusse, A., and Echard, A. (2016). Rab35 GTPase couples cell division with initiation of epithelial apico-basal polarity and lumen opening. Nat Commun *7*, 11166. 10.1038/ncomms11166.
25. Bisi, S., Marchesi, S., Rizvi, A., Carra, D., Beznoussenko, G.V., Ferrara, I., Deflorian, G., Mironov, A., Bertalot, G., Pisati, F., et al. (2020). IRSp53 controls plasma membrane shape and polarized transport at the nascent lumen in epithelial tubules. Nat Commun *11*, 3516. 10.1038/s41467-020-17091-x.
26. Strilic, B., Eglinger, J., Krieg, M., Zeeb, M., Axnick, J., Babal, P., Muller, D.J., and Lammert, E. (2010). Electrostatic cell-surface repulsion initiates lumen formation in developing blood vessels. Curr Biol *20*, 2003-2009. 10.1016/j.cub.2010.09.061.
27. Mukenhirn, M., Wang, C.H., Guyomar, T., Bovyn, M.J., Staddon, M.F., van der Veen, R.E., Maraspini, R., Lu, L., Martin-Lemaitre, C., Sano, M., et al. (2024). Tight junctions control lumen morphology via hydrostatic pressure and junctional tension. Dev Cell *59*, 2866-2881 e2868. 10.1016/j.devcel.2024.07.016.
28. Tepass, U. (2012). The apical polarity protein network in Drosophila epithelial cells: regulation of polarity, junctions, morphogenesis, cell growth, and

survival. Annu Rev Cell Dev Biol *28*, 655-685. 10.1146/annurev-cellbio-092910-154033.
29. Margolis, B. (2018). The Crumbs3 Polarity Protein. Cold Spring Harb Perspect Biol *10*. 10.1101/cshperspect.a027961.
30. Whiteman, E.L., Fan, S., Harder, J.L., Walton, K.D., Liu, C.J., Soofi, A., Fogg, V.C., Hershenson, M.B., Dressler, G.R., Deutsch, G.H., et al. (2014). Crumbs3 is essential for proper epithelial development and viability. Molecular and cellular biology *34*, 43-56. 10.1128/MCB.00999-13.
31. Charrier, L.E., Loie, E., and Laprise, P. (2015). Mouse Crumbs3 sustains epithelial tissue morphogenesis in vivo. Scientific reports *5*, 17699. 10.1038/srep17699.
32. Weide, T., Vollenbroker, B., Schulze, U., Djuric, I., Edeling, M., Bonse, J., Hochapfel, F., Panichkina, O., Wennmann, D.O., George, B., et al. (2017). Pals1 Haploinsufficiency Results in Proteinuria and Cyst Formation. Journal of the American Society of Nephrology : JASN *28*, 2093-2107. 10.1681/ASN.2016040474.
33. Shin, K., Straight, S., and Margolis, B. (2005). PATJ regulates tight junction formation and polarity in mammalian epithelial cells. The Journal of cell biology *168*, 705-711. jcb.200408064 [pii]. 10.1083/jcb.200408064.
34. Straight, S.W., Shin, K., Fogg, V.C., Fan, S., Liu, C.J., Roh, M., and Margolis, B. (2004). Loss of PALS1 expression leads to tight junction and polarity defects. Molecular biology of the cell *15*, 1981-1990. 10.1091/mbc.E03-08-0620. E03-08-0620 [pii].
35. Roh, M.H., Fan, S., Liu, C.J., and Margolis, B. (2003). The Crumbs3-Pals1 complex participates in the establishment of polarity in mammalian epithelial cells. Journal of cell science *116*, 2895-2906. 10.1242/jcs.00500. jcs.00500 [pii].
36. Schluter, M.A., Pfarr, C.S., Pieczynski, J., Whiteman, E.L., Hurd, T.W., Fan, S., Liu, C.J., and Margolis, B. (2009). Trafficking of Crumbs3 during cytokinesis is crucial for lumen formation. Molecular biology of the cell *20*, 4652-4663. 10.1091/mbc.E09-02-0137.
37. Torkko, J.M., Manninen, A., Schuck, S., and Simons, K. (2008). Depletion of apical transport proteins perturbs epithelial cyst formation and ciliogenesis. Journal of cell science *121*, 1193-1203. 10.1242/jcs.015495.
38. Pombo-Garcia, K., Adame-Arana, O., Martin-Lemaitre, C., Julicher, F., and Honigmann, A. (2024). Membrane prewetting by condensates promotes tight-junction belt formation. Nature *632*, 647-655. 10.1038/s41586-024-07726-0.
39. Tan, B., Yatim, S., Peng, S., Gunaratne, J., Hunziker, W., and Ludwig, A. (2020). The Mammalian Crumbs Complex Defines a Distinct Polarity Domain Apical of Epithelial Tight Junctions. Curr Biol *30*, 2791-2804 e2796. 10.1016/j.cub.2020.05.032.
40. Groh, A.C., Moller-Kerutt, A., Gilhaus, K., Hoffken, V., Nedvetsky, P., Kleimann, S., Behrens, M., Ghosh, S., Hansen, U., Krahn, M.P., et al. (2024). PALS1 is a key regulator of the lateral distribution of tight junction proteins in renal epithelial cells. Journal of cell science *137*. 10.1242/jcs.261303.
41. Lam, S.S., Martell, J.D., Kamer, K.J., Deerinck, T.J., Ellisman, M.H., Mootha, V.K., and Ting, A.Y. (2015). Directed evolution of APEX2 for electron microscopy and proximity labeling. Nature methods *12*, 51-54. 10.1038/nmeth.3179.

42. Martin, E., Girardello, R., Dittmar, G., and Ludwig, A. (2021). New insights into the organization and regulation of the apical polarity network in mammalian epithelial cells. The FEBS journal. 10.1111/febs.15710.
43. Vega-Salas, D.E., Salas, P.J., and Rodriguez-Boulan, E. (1988). Exocytosis of vacuolar apical compartment (VAC): a cell-cell contact controlled mechanism for the establishment of the apical plasma membrane domain in epithelial cells. The Journal of cell biology *107*, 1717-1728. 10.1083/jcb.107.5.1717.
44. Vega-Salas, D.E., Salas, P.J., and Rodriguez-Boulan, E. (1987). Modulation of the expression of an apical plasma membrane protein of Madin-Darby canine kidney epithelial cells: cell-cell interactions control the appearance of a novel intracellular storage compartment. The Journal of cell biology *104*, 1249-1259. 10.1083/jcb.104.5.1249.
45. Ludwig, A. (2020). Selective Visualization of Caveolae by TEM Using APEX2. Methods in molecular biology *2169*, 1-10. 10.1007/978-1-0716-0732-9_1.
46. Tan, B., Peng, S., Yatim, S., Gunaratne, J., Hunziker, W., and Ludwig, A. (2020). An Optimized Protocol for Proximity Biotinylation in Confluent Epithelial Cell Cultures Using the Peroxidase APEX2. STAR Protoc *1*, 100074. 10.1016/j.xpro.2020.100074.
47. Mangeol, P., Massey-Harroche, D., Richard, F., Concordet, J.P., Lenne, P.F., and Le Bivic, A. (2022). Super-resolution imaging uncovers the nanoscopic segregation of polarity proteins in epithelia. eLife *11*. 10.7554/eLife.62087.
48. Li, J.X.H., Tang, V.W., and Brieher, W.M. (2020). Actin protrusions push at apical junctions to maintain E-cadherin adhesion. Proceedings of the National Academy of Sciences of the United States of America *117*, 432-438. 10.1073/pnas.1908654117.
49. Silver, J.T., Wirtz-Peitz, F., Simoes, S., Pellikka, M., Yan, D., Binari, R., Nishimura, T., Li, Y., Harris, T.J.C., Perrimon, N., and Tepass, U. (2019). Apical polarity proteins recruit the RhoGEF Cysts to promote junctional myosin assembly. The Journal of cell biology *218*, 3397-3414. 10.1083/jcb.201807106.
50. Simoes, S., Lerchbaumer, G., Pellikka, M., Giannatou, P., Lam, T., Kim, D., Yu, J., Ter Stal, D., Al Kakouni, K., Fernandez-Gonzalez, R., and Tepass, U. (2022). Crumbs complex-directed apical membrane dynamics in epithelial cell ingression. The Journal of cell biology *221*. 10.1083/jcb.202108076.
51. Roper, K. (2012). Anisotropy of Crumbs and aPKC drives myosin cable assembly during tube formation. Dev Cell *23*, 939-953. 10.1016/j.devcel.2012.09.013.
52. Sidor, C., Stevens, T.J., Jin, L., Boulanger, J., and Roper, K. (2020). Rho-Kinase Planar Polarization at Tissue Boundaries Depends on Phospho-regulation of Membrane Residence Time. Dev Cell *52*, 364-378 e367. 10.1016/j.devcel.2019.12.003.
53. Terry, S.J., Zihni, C., Elbediwy, A., Vitiello, E., Leefa Chong San, I.V., Balda, M.S., and Matter, K. (2011). Spatially restricted activation of RhoA signalling at epithelial junctions by p114RhoGEF drives junction formation and morphogenesis. Nature cell biology *13*, 159-166. 10.1038/ncb2156.
54. Nakajima, H., and Tanoue, T. (2011). Lulu2 regulates the circumferential actomyosin tensile system in epithelial cells through p114RhoGEF. The Journal of cell biology *195*, 245-261. 10.1083/jcb.201104118.
55. Cencer, C.S., Silverman, J.B., Meenderink, L.M., Krystofiak, E.S., Millis, B.A., and Tyska, M.J. (2023). Adhesion-based capture stabilizes nascent microvilli

at epithelial cell junctions. Dev Cell *58*, 2048-2062 e2047. 10.1016/j.devcel.2023.09.001.
56. Ebnet, K., Suzuki, A., Horikoshi, Y., Hirose, T., Meyer Zu Brickwedde, M.K., Ohno, S., and Vestweber, D. (2001). The cell polarity protein ASIP/PAR-3 directly associates with junctional adhesion molecule (JAM). The EMBO journal *20*, 3738-3748. 10.1093/emboj/20.14.3738.
57. Ebnet, K., Schulz, C.U., Meyer Zu Brickwedde, M.K., Pendl, G.G., and Vestweber, D. (2000). Junctional adhesion molecule interacts with the PDZ domain-containing proteins AF-6 and ZO-1. The Journal of biological chemistry *275*, 27979-27988. 10.1074/jbc.M002363200.
58. Hazelett, C.C., Sheff, D., and Yeaman, C. (2011). RalA and RalB differentially regulate development of epithelial tight junctions. Molecular biology of the cell *22*, 4787-4800. 10.1091/mbc.E11-07-0657.
59. Ahmed, S.M., and Macara, I.G. (2017). The Par3 polarity protein is an exocyst receptor essential for mammary cell survival. Nat Commun *8*, 14867. 10.1038/ncomms14867.
60. Yeaman, C., Grindstaff, K.K., and Nelson, W.J. (2004). Mechanism of recruiting Sec6/8 (exocyst) complex to the apical junctional complex during polarization of epithelial cells. Journal of cell science *117*, 559-570. 10.1242/jcs.00893.
61. Grindstaff, K.K., Yeaman, C., Anandasabapathy, N., Hsu, S.C., Rodriguez-Boulan, E., Scheller, R.H., and Nelson, W.J. (1998). Sec6/8 complex is recruited to cell-cell contacts and specifies transport vesicle delivery to the basal-lateral membrane in epithelial cells. Cell *93*, 731-740.
62. Citi, S., Guerrera, D., Spadaro, D., and Shah, J. (2014). Epithelial junctions and Rho family GTPases: the zonular signalosome. Small GTPases *5*, 1-15. 10.4161/21541248.2014.973760.
63. Mack, N.A., and Georgiou, M. (2014). The interdependence of the Rho GTPases and apicobasal cell polarity. Small GTPases *5*, 10. 10.4161/21541248.2014.973768.
64. Hodge, R.G., and Ridley, A.J. (2016). Regulating Rho GTPases and their regulators. Nat Rev Mol Cell Biol *17*, 496-510. 10.1038/nrm.2016.67.
65. Popoff, M.R., and Geny, B. (2009). Multifaceted role of Rho, Rac, Cdc42 and Ras in intercellular junctions, lessons from toxins. Biochimica et biophysica acta *1788*, 797-812. 10.1016/j.bbamem.2009.01.011.
66. Zihni, C., and Terry, S.J. (2015). RhoGTPase signalling at epithelial tight junctions: Bridging the GAP between polarity and cancer. The international journal of biochemistry & cell biology *64*, 120-125. 10.1016/j.biocel.2015.02.020.
67. Pichaud, F., Walther, R.F., and Nunes de Almeida, F. (2019). Regulation of Cdc42 and its effectors in epithelial morphogenesis. Journal of cell science *132*. 10.1242/jcs.217869.
68. Yamada, S., and Nelson, W.J. (2007). Localized zones of Rho and Rac activities drive initiation and expansion of epithelial cell-cell adhesion. The Journal of cell biology *178*, 517-527. 10.1083/jcb.200701058.
69. Daneshjou, N., Sieracki, N., van Nieuw Amerongen, G.P., Conway, D.E., Schwartz, M.A., Komarova, Y.A., and Malik, A.B. (2015). Rac1 functions as a reversible tension modulator to stabilize VE-cadherin trans-interaction. The Journal of cell biology *208*, 23-32. 10.1083/jcb.201409108.

70. Ando, K., Fukuhara, S., Moriya, T., Obara, Y., Nakahata, N., and Mochizuki, N. (2013). Rap1 potentiates endothelial cell junctions by spatially controlling myosin II activity and actin organization. The Journal of cell biology *202*, 901-916. 10.1083/jcb.201301115.
71. Post, A., Pannekoek, W.J., Ross, S.H., Verlaan, I., Brouwer, P.M., and Bos, J.L. (2013). Rasip1 mediates Rap1 regulation of Rho in endothelial barrier function through ArhGAP29. Proceedings of the National Academy of Sciences of the United States of America *110*, 11427-11432. 10.1073/pnas.1306595110.
72. Monteiro, A.C., Sumagin, R., Rankin, C.R., Leoni, G., Mina, M.J., Reiter, D.M., Stehle, T., Dermody, T.S., Schaefer, S.A., Hall, R.A., et al. (2013). JAM-A associates with ZO-2, afadin, and PDZ-GEF1 to activate Rap2c and regulate epithelial barrier function. Molecular biology of the cell *24*, 2849-2860. 10.1091/mbc.E13-06-0298.
73. Beutel, O., Maraspini, R., Pombo-Garcia, K., Martin-Lemaitre, C., and Honigmann, A. (2019). Phase Separation of Zonula Occludens Proteins Drives Formation of Tight Junctions. Cell *179*, 923-936 e911. 10.1016/j.cell.2019.10.011.
74. Sun, D., Zhao, X., Wiegand, T., Martin-Lemaitre, C., Borianne, T., Kleinschmidt, L., Grill, S.W., Hyman, A.A., Weber, C., and Honigmann, A. (2024). Assembly of tight junction belts by ZO1 surface condensation and local actin polymerization. Dev Cell. 10.1016/j.devcel.2024.12.012.
75. Bryant, D.M., Roignot, J., Datta, A., Overeem, A.W., Kim, M., Yu, W., Peng, X., Eastburn, D.J., Ewald, A.J., Werb, Z., and Mostov, K.E. (2014). A molecular switch for the orientation of epithelial cell polarization. Dev Cell *31*, 171-187. 10.1016/j.devcel.2014.08.027.
76. Brignoni, M., Podesta, E.J., Mele, P., Rodriguez, M.L., Vega-Salas, D.E., and Salas, P.J. (1993). Exocytosis of vacuolar apical compartment (VAC) in Madin-Darby canine kidney epithelial cells: cAMP is involved as second messenger. Exp Cell Res *205*, 171-178. 10.1006/excr.1993.1072.
77. Vega-Salas, D.E., San Martino, J.A., Salas, P.J., and Baldi, A. (1993). Vacuolar apical compartment (VAC) in breast carcinoma cell lines (MCF-7 and T47D): failure of the cell-cell regulated exocytosis mechanism of apical membrane. Differentiation *54*, 131-141. 10.1111/j.1432-0436.1993.tb00716.x.
78. Low, S.H., Miura, M., Roche, P.A., Valdez, A.C., Mostov, K.E., and Weimbs, T. (2000). Intracellular redirection of plasma membrane trafficking after loss of epithelial cell polarity. Molecular biology of the cell *11*, 3045-3060. 10.1091/mbc.11.9.3045.
79. Taniguchi, K., Shao, Y., Townshend, R.F., Cortez, C.L., Harris, C.E., Meshinchi, S., Kalantry, S., Fu, J., O'Shea, K.S., and Gumucio, D.L. (2017). An apicosome initiates self-organizing morphogenesis of human pluripotent stem cells. The Journal of cell biology *216*, 3981-3990. 10.1083/jcb.201704085.
80. Wang, S., Lin, C.W., Carleton, A.E., Cortez, C.L., Johnson, C., Taniguchi, L.E., Sekulovski, N., Townshend, R.F., Basrur, V., Nesvizhskii, A.I., et al. (2021). Spatially resolved cell polarity proteomics of a human epiblast model. Sci Adv *7*. 10.1126/sciadv.abd8407.
81. Gredler, M.L., and Zallen, J.A. (2023). Multicellular rosettes link mesenchymal-epithelial transition to radial intercalation in the mouse axial mesoderm. Dev Cell *58*, 933-950 e935. 10.1016/j.devcel.2023.03.018.

82. Kesavan, G., Sand, F.W., Greiner, T.U., Johansson, J.K., Kobberup, S., Wu, X., Brakebusch, C., and Semb, H. (2009). Cdc42-mediated tubulogenesis controls cell specification. Cell *139*, 791-801. 10.1016/j.cell.2009.08.049.
83. Schneeberger, K., Vogel, G.F., Teunissen, H., van Ommen, D.D., Begthel, H., El Bouazzaoui, L., van Vugt, A.H., Beekman, J.M., Klumperman, J., Muller, T., et al. (2015). An inducible mouse model for microvillus inclusion disease reveals a role for myosin Vb in apical and basolateral trafficking. Proceedings of the National Academy of Sciences of the United States of America *112*, 12408-12413. 10.1073/pnas.1516672112.
84. Chen, J., and St Johnston, D. (2022). De novo apical domain formation inside the Drosophila adult midgut epithelium. eLife *11*. 10.7554/eLife.76366.
85. Galenza, A., Moreno-Roman, P., Su, Y.H., Acosta-Alvarez, L., Debec, A., Guichet, A., Knapp, J.M., Kizilyaprak, C., Humbel, B.M., Kolotuev, I., and O'Brien, L.E. (2023). Basal stem cell progeny establish their apical surface in a junctional niche during turnover of an adult barrier epithelium. Nature cell biology *25*, 658-671. 10.1038/s41556-023-01116-w.
86. Horikoshi, Y., Suzuki, A., Yamanaka, T., Sasaki, K., Mizuno, K., Sawada, H., Yonemura, S., and Ohno, S. (2009). Interaction between PAR-3 and the aPKC-PAR-6 complex is indispensable for apical domain development of epithelial cells. Journal of cell science *122*, 1595-1606. 10.1242/jcs.043174.
87. Ferrari, A., Veligodskiy, A., Berge, U., Lucas, M.S., and Kroschewski, R. (2008). ROCK-mediated contractility, tight junctions and channels contribute to the conversion of a preapical patch into apical surface during isochoric lumen initiation. Journal of cell science *121*, 3649-3663. 10.1242/jcs.018648.
88. Cohen, D., Brennwald, P.J., Rodriguez-Boulan, E., and Musch, A. (2004). Mammalian PAR-1 determines epithelial lumen polarity by organizing the microtubule cytoskeleton. The Journal of cell biology *164*, 717-727. 10.1083/jcb.200308104.
89. Li, Y., Wei, Z., Yan, Y., Wan, Q., Du, Q., and Zhang, M. (2014). Structure of Crumbs tail in complex with the PALS1 PDZ-SH3-GK tandem reveals a highly specific assembly mechanism for the apical Crumbs complex. Proceedings of the National Academy of Sciences of the United States of America *111*, 17444-17449. 10.1073/pnas.1416515111.
90. Indana, D., Zakharov, A., Lim, Y., Dunn, A.R., Bhutani, N., Shenoy, V.B., and Chaudhuri, O. (2024). Lumen expansion is initially driven by apical actin polymerization followed by osmotic pressure in a human epiblast model. Cell stem cell *31*, 640-656 e648. 10.1016/j.stem.2024.03.016.
91. Loie, E., Charrier, L.E., Sollier, K., Masson, J.Y., and Laprise, P. (2015). CRB3A Controls the Morphology and Cohesion of Cancer Cells through Ehm2/p114RhoGEF-Dependent Signaling. Molecular and cellular biology *35*, 3423-3435. 10.1128/MCB.00673-15.
92. Schindelin, J., Arganda-Carreras, I., Frise, E., Kaynig, V., Longair, M., Pietzsch, T., Preibisch, S., Rueden, C., Saalfeld, S., Schmid, B., et al. (2012). Fiji: an open-source platform for biological-image analysis. Nature methods *9*, 676-682. 10.1038/nmeth.2019.
93. Schneider, C.A., Rasband, W.S., and Eliceiri, K.W. (2012). NIH Image to ImageJ: 25 years of image analysis. Nature methods *9*, 671-675. 10.1038/nmeth.2089.

94. Martin, E., Girardello, R., Dittmar, G., and Ludwig, A. (2024). Time-resolved proximity proteomics uncovers a membrane tension-sensitive caveolin-1 interactome at the rear of migrating cells. eLife *13*. 10.7554/eLife.85601.
95. Tapia, J.C., Kasthuri, N., Hayworth, K.J., Schalek, R., Lichtman, J.W., Smith, S.J., and Buchanan, J. (2012). High-contrast en bloc staining of neuronal tissue for field emission scanning electron microscopy. Nat Protoc *7*, 193-206. 10.1038/nprot.2011.439.
96. Stringer, C., Wang, T., Michaelos, M., and Pachitariu, M. (2021). Cellpose: a generalist algorithm for cellular segmentation. Nature methods *18*, 100-106. 10.1038/s41592-020-01018-x.

Figures:

Figure 1: Pals1 and apical cargo are delivered to nascent cell-cell contacts via VACs

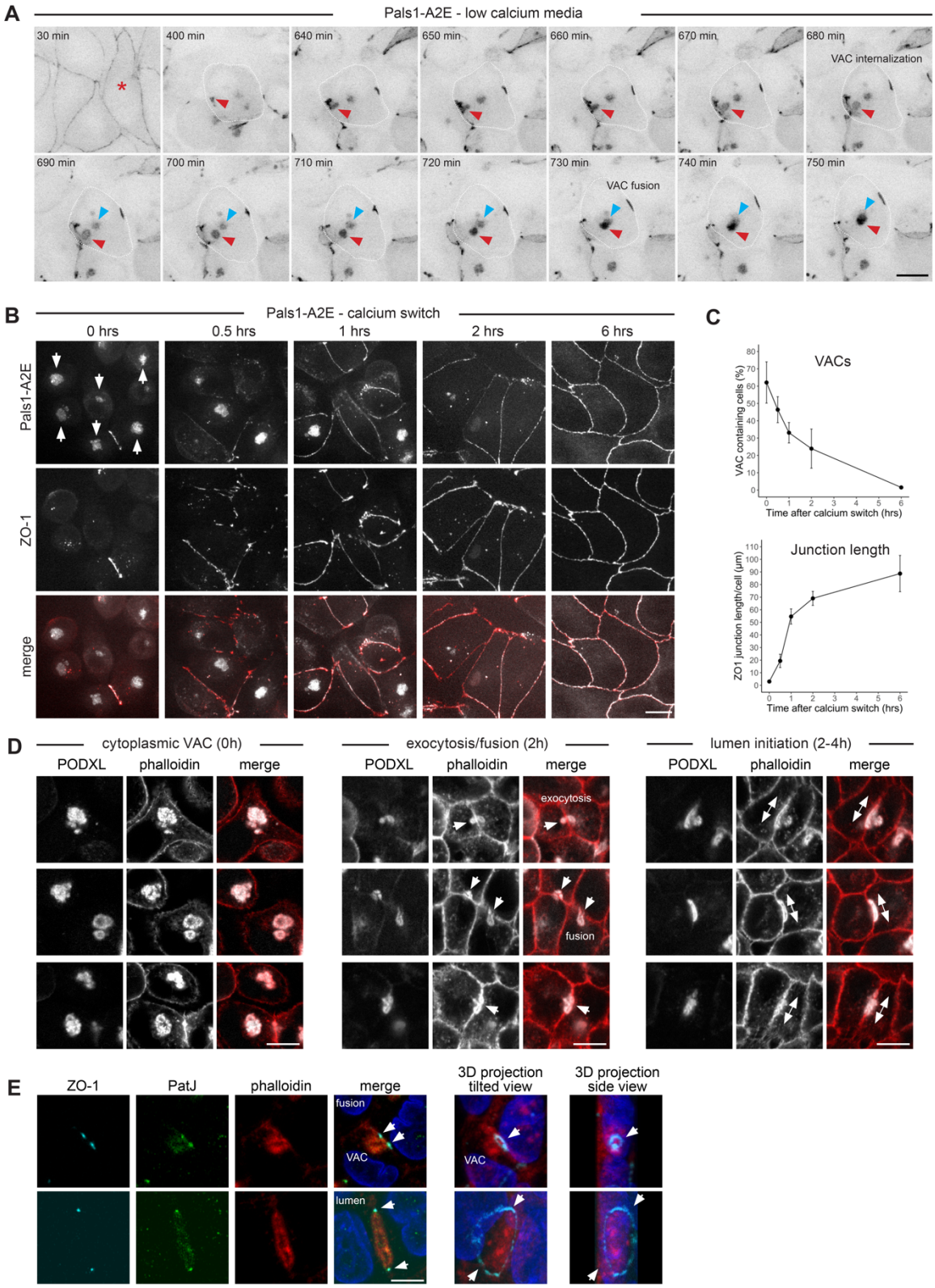

Figure 1: Pals1 and apical cargo are delivered to nascent cell-cell contacts via vacuolar apical compartments (VACs)
(A) Time-lapse imaging of MDCK-II cells stably expressing Pals1-A2E upon calcium withdrawal. Pals1 is internalized into large organelles (VACs). Fusion events between individual VACs are observed (red and blue arrowhead). Scale bar 5 µm.
(B) Calcium switch assay in Pals1-A2E cells. Cells were fixed at the indicated time points post-calcium addition and stained with antibodies against ZO-1. Scale bar 5 µm.
(C) Quantification of tight junction length and the number of VACs based on the data shown in (B). Data is expressed as mean +/- SD (n=115-167 for each time point).
(D) MDCK-II cells were fixed at 0h or 2h post calcium addition and stained with anti-PODXL antibodies and phalloidin. Intracellular VACs (left), VAC fusion events with the lateral membrane (middle), and lateral lumens (right) were observed. Scale bar 5 µm.
(D) MDCK-II cells were fixed at 2h post calcium addition and stained with anti-ZO-1 and anti-PatJ antibodies and phalloidin. Single confocal sections of VAC fusion events (top) and lateral lumens (bottom) are shown. 3D projections show the overlay of phalloidin and ZO-1 signals. Scale bar 2.5 µm.

Figure 2: Ultrastructural analysis of VAC exocytosis and VMZ formation

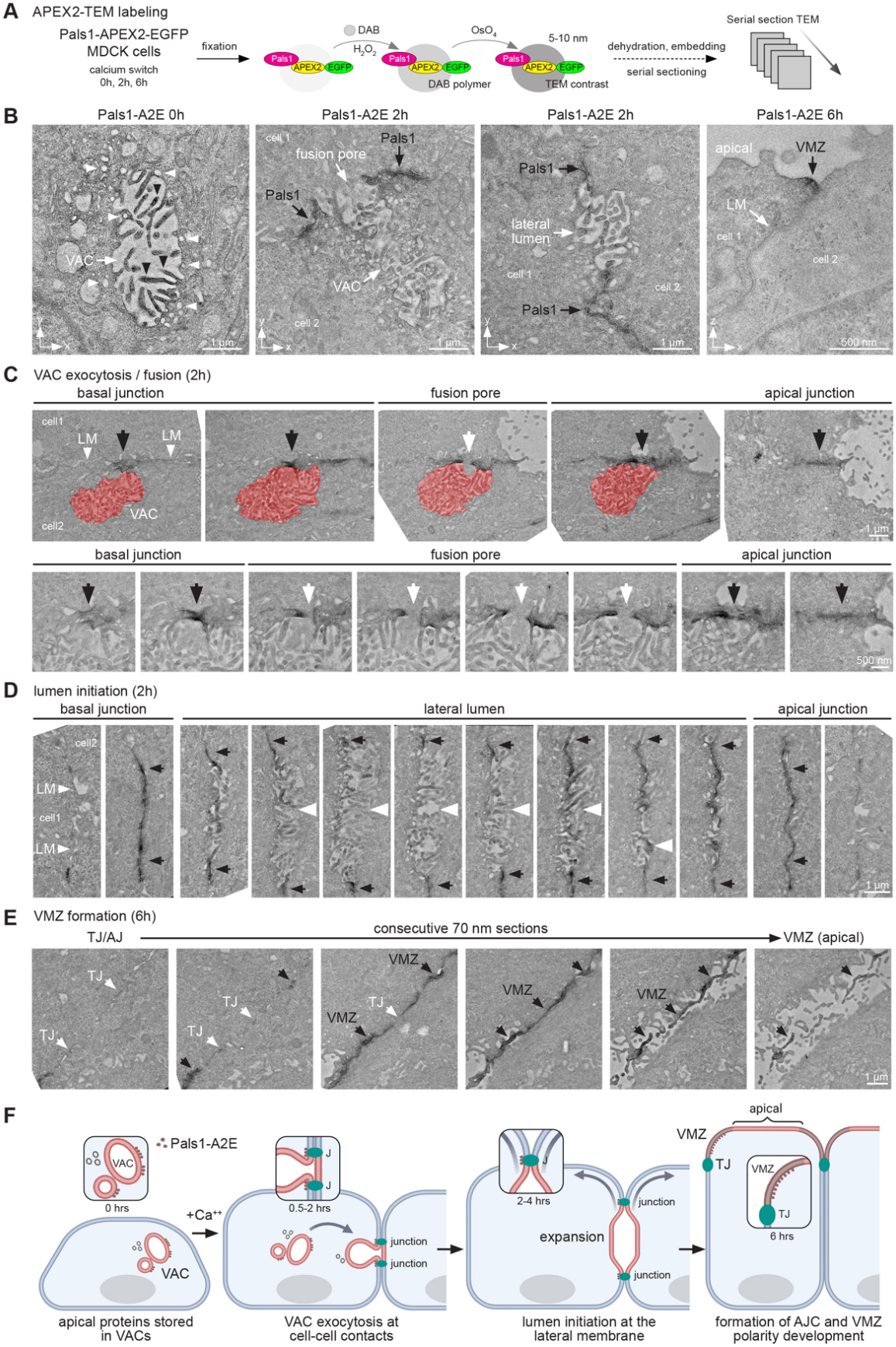

Figure 2: Ultrastructural analysis of VAC exocytosis and VMZ formation
(A) Principle of APEX2-TEM labeling. A brief (2-5 min) incubation of fixed cells with diaminobenzidine (DAB) and hydrogen peroxide (H_2O_2) results in the deposition of a DAB polymer that upon binding to OsO_4 produces an electron-dense stain.
(B) APEX2 TEM labeling of Pals1-A2E at different time points of the calcium switch assay. White arrowheads indicate small vesicles close to VACs, black arrowheads indicate enhanced contrast of microvilli inside the VACs produced by APEX2 labeling. LM = lateral membrane.
(C) Representative serial section TEM of a VAC fusion event with the lateral membrane. Select serial sections of the volume are shown. Note the increase in junctional EM contrast produced by Pals1-A2E (black arrowhead) around the VAC fusion site (white arrowhead).
(D) Representative serial section TEM of a lateral lumen. Select serial sections of the volume are shown. Note the increase in junctional EM contrast produced by Pals1-A2E (black arrowhead) around the lumen (white arrowhead).
(E) Representative serial section TEM of Pals1-A2E at 6h post-calcium addition. Samples were sectioned *en face* (parallel to the substratum). Consecutive serial sections of the apical/lateral interface are shown. Note the increase in EM contrast produced by Pals1-A2E (black arrowhead) apical of TJs (white arrowhead).
(F) Model of lateral lumen formation and polarity development in the calcium switch assay.

Figure 3: Proximity proteomics resolves distinct stages of cell junction assembly

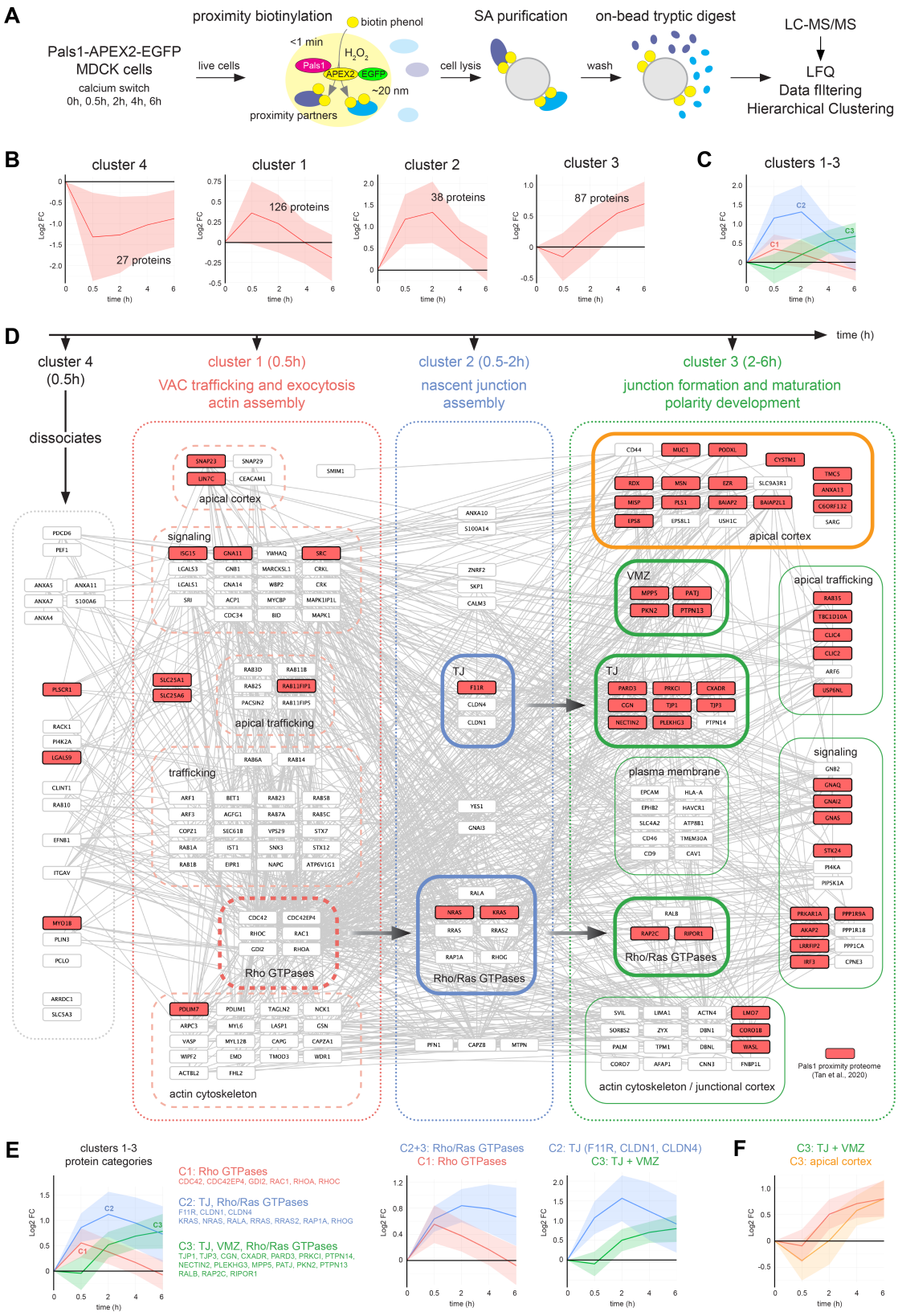

Figure 3: Proximity proteomics resolves distinct stages of cell-cell junction assembly

(A) Principle of proximity biotinylation with APEX2 and workflow used to generate a time-resolved proteome of Pals1 during cell-cell junction assembly in the calcium switch assay. Live cells expressing Pals1-A2E are incubated with biotin phenol for 30 min followed by the addition of H_2O_2 for 1 min. This results in the biotinylation of proteins in a radius of ~20 nm. Upon cell lysis, biotinylated proteins are isolated using streptavidin (SA) pulldowns and analysed by liquid chromatography tandem mass spectrometry (LC-MS/MS).

(B) Hierarchical clustering of the 278 identified proteins reveals four clusters with distinct kinetics. Data is expressed as mean +/- SD.

(C) Direct comparison of the kinetics of clusters 1-3.

(D) Temporally resolved protein interaction network of Pals1 during cell-cell junction assembly based on STRING and BioGRID entries. A total of 200 proteins (out of 278 identified) are shown. Proteins were categorized based on known functions and our previously defined proteome of the apical-lateral border [39]. Proteins highlighted in red are core components of the static Pals1 proteome identified in Tan et al., [39].

(E) Kinetics of Rho and Ras GTPases, TJ proteins and VMZ proteins.

(F) Kinetics of TJ and VMZ proteins and proteins residing at the apical cortex.

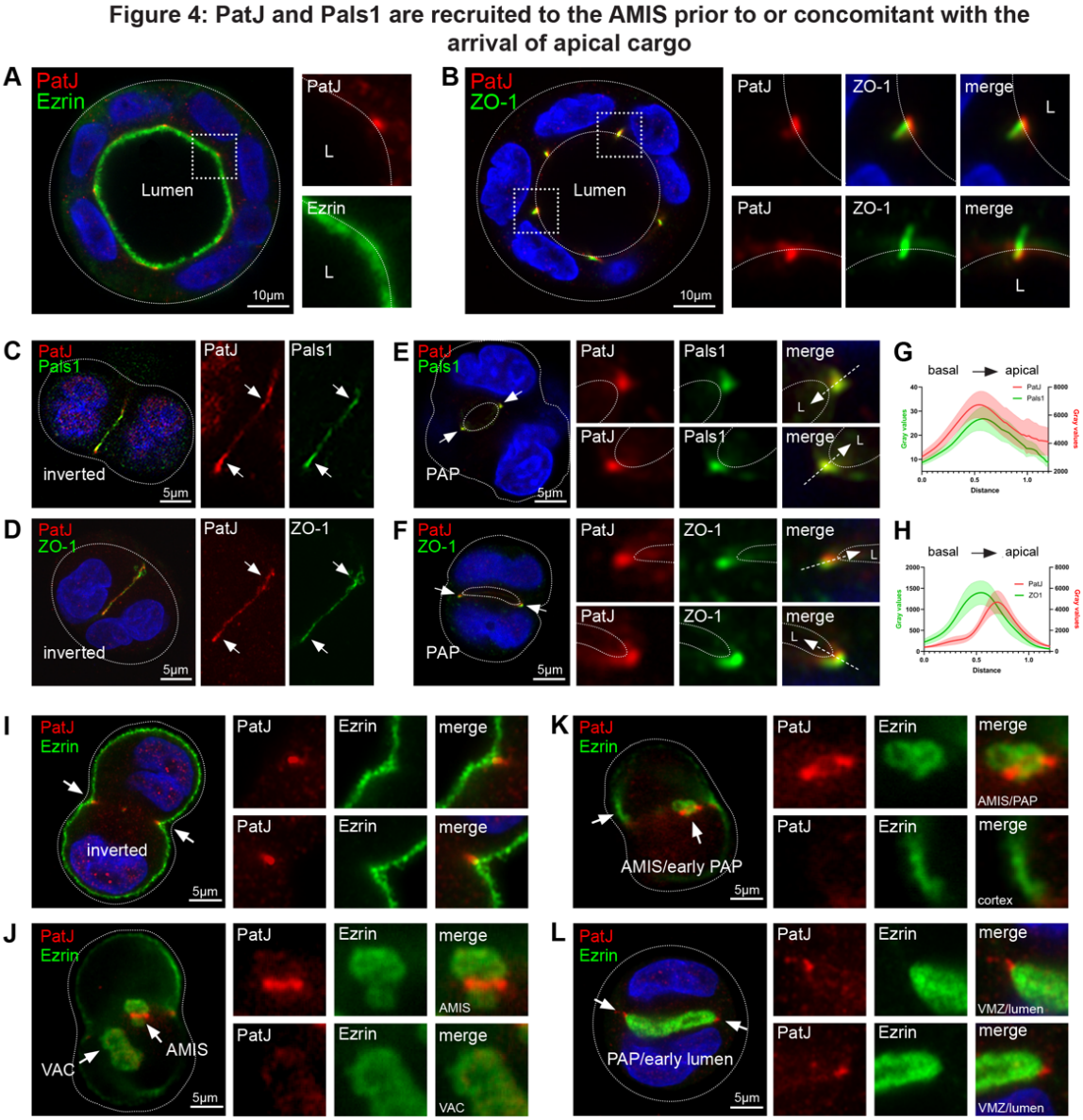

Figure 4: PatJ and Pals1 are recruited to the AMIS prior to or concomitant with the arrival of apical cargo

(A and B) Representative Airyscan images of MDCK-II cell cysts grown in Matrigel for 4 days stained with anti-PatJ and anti-ezrin antibodies (A) or with anti-PatJ and anti-ZO-1 antibodies (B). Note that PatJ localizes apical of ZO-1 (insets in B).
(C and D) Representative Airyscan images of MDCK-II cells in the inverted stage. Cells were fixed at 16h in Matrigel and costained with anti-PatJ and anti-Pals1 antibodies (C) or with anti-PatJ and anti-ZO-1 antibodies (D).
(E and F) Representative Airyscan images of MDCK-II cells in the PAP stage (24h). Cells were fixed at 24h in Matrigel and costained with anti-PatJ and anti-Pals1 antibodies (E) or with anti-PatJ and anti-ZO-1 antibodies (F). Arrows in the insets highlight the direction of the line scan analysis shown in (G and H).
(G and H) Line scan quantification of data shown in (E and F). n=10 line scans. Data is expressed as mean +/- SD.
(I-L) Representative Airyscan images of MDCK-II cells in the inverted (I), AMIS (J), early PAP (K), and PAP/open lumen (L) stages. Cells were stained with anti-PatJ and

anti-ezrin antibodies. An intracellular VAC (J) and potential VAC fusion events with the AMIS (J and K) are shown. Arrowheads highlight areas magnified in the insets.

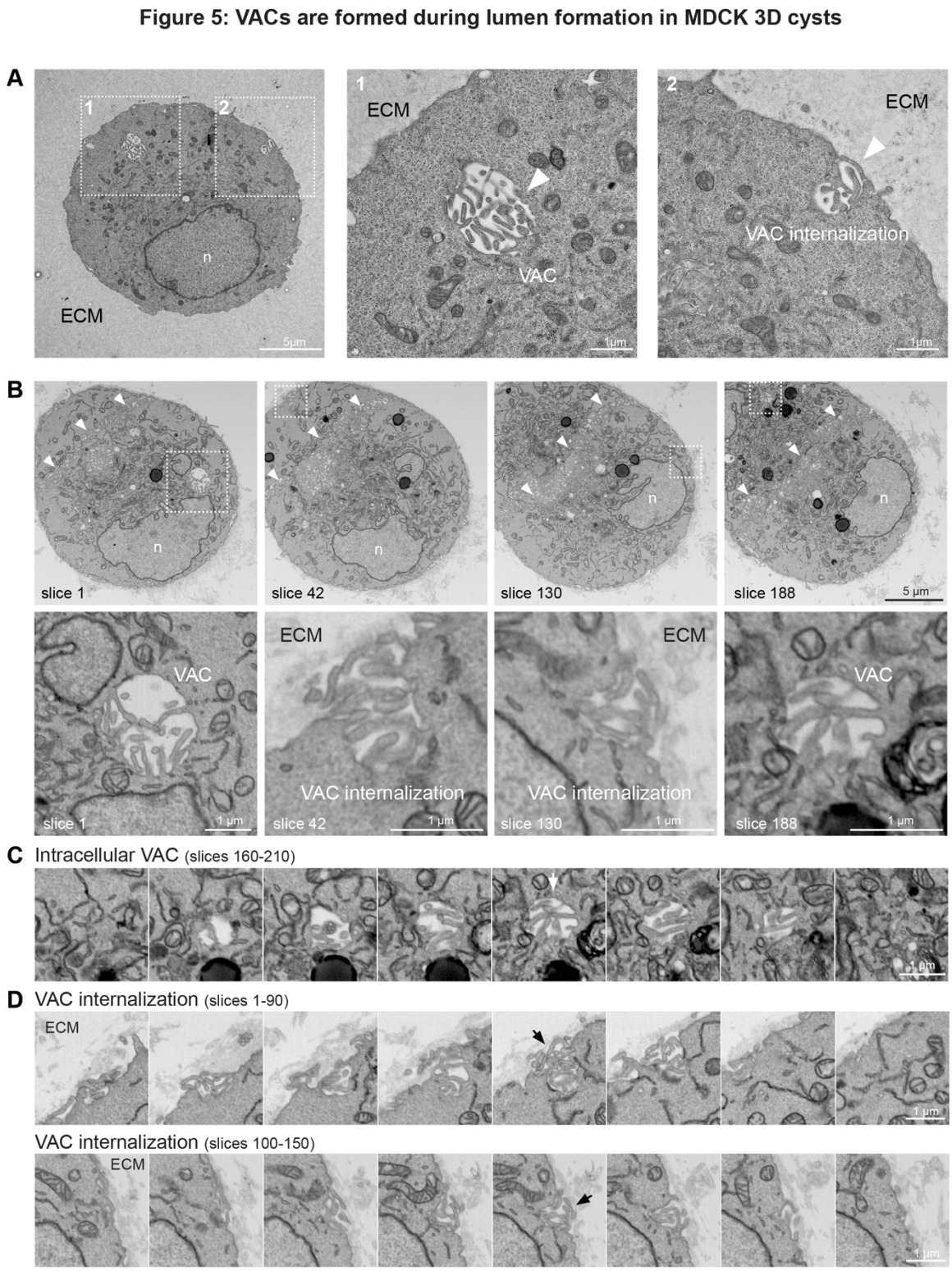

Figure 5: VACs are formed during lumen formation in MDCK 3D cysts
(A) Representative TEM image of MDCK cells embedded in Matrigel for 18h. An intracellular VAC and a potential VAC internalization event at the ECM-facing plasma membrane are shown. n=nucleus
(B-E) FIB-SEM of MDCK cells embedded in Matrigel for 24h.

(B) Representative slices through the FIB-SEM volume. White arrowheads demarcate the cell-cell contact site. n=nucleus. Magnified views of intracellular VACs and sites of VAC internalization at the ECM-facing plasma membrane are shown.
(C) Sequential FIB-SEM images of an intracellular VAC (white arrow). See also Movie S1.
(D) Sequential FIB-SEM images of two potential VAC internalization events (black arrow). See also Movies S2 and S3.

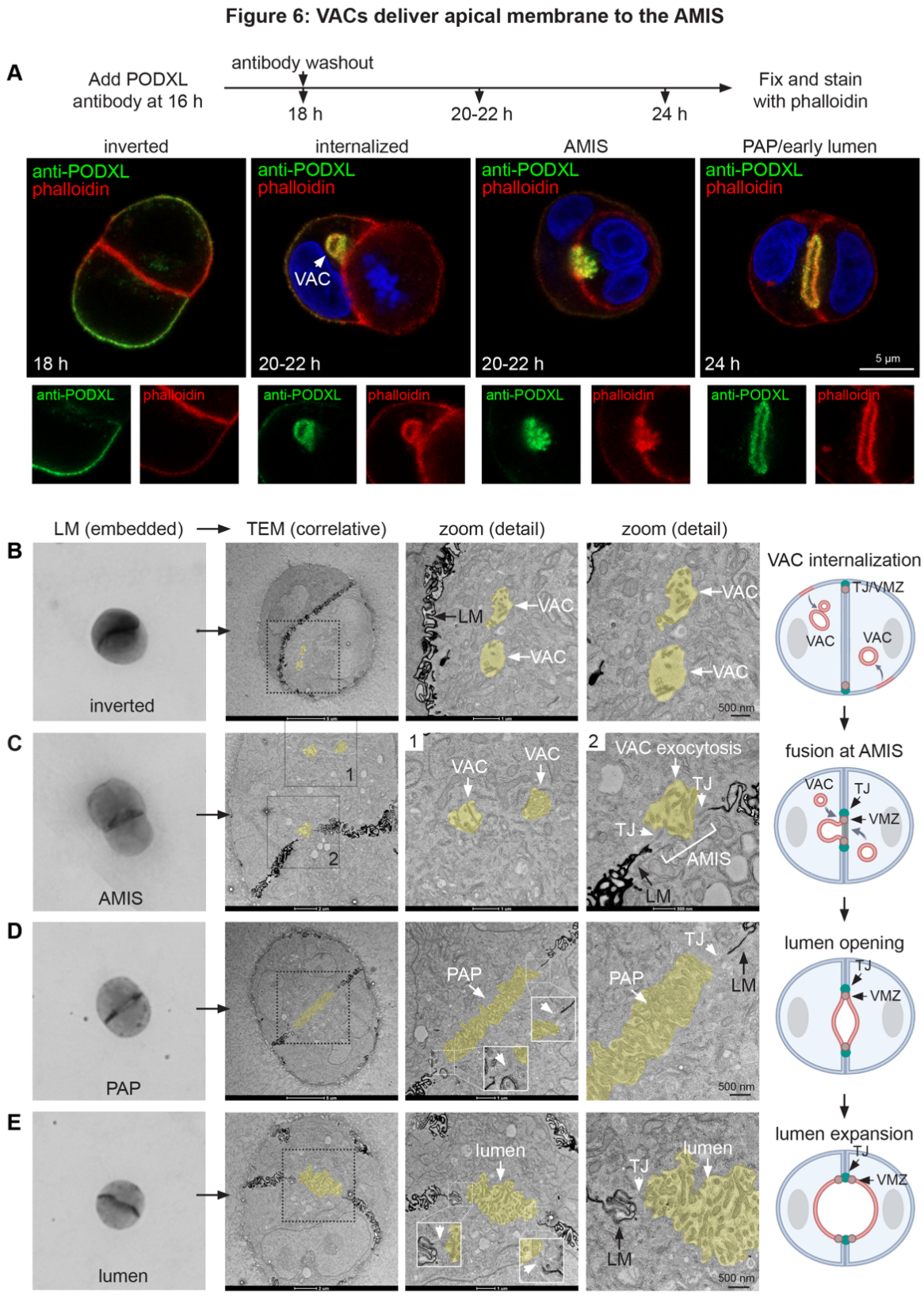

Figure 6: VACs deliver apical membrane to the AMIS
(A) The trafficking of PODXL was analysed using an antibody uptake assay. MDCK-II cells embedded in Matrigel for 16h were incubated with PODXL antibody for 2h, followed by washout at 18h. Cells were fixed between 18h and 24h, incubated with a

fluorescently labeled secondary antibody to detect the PODXL antibody, and costained with phalloidin. Representative Airyscan images are shown. Note that PODXL localizes to VACs.
(B-E) MDCK cells embedded in Matrigel for 24h were processed for correlative light and serial section TEM. Inverted (B), AMIS (C), PAP (D), and open lumen (E) stages were identified. Transmitted light images (left column) and representative correlative TEM micrographs are shown. The EM contrast of the lateral membrane (LM) was enhanced by tannic acid impregnation. The apical lumen is surrounded by TJs, which appear electron lucent. Intracellular VACs (B, C) and a VAC fusion event at the AMIS (C) were observed.

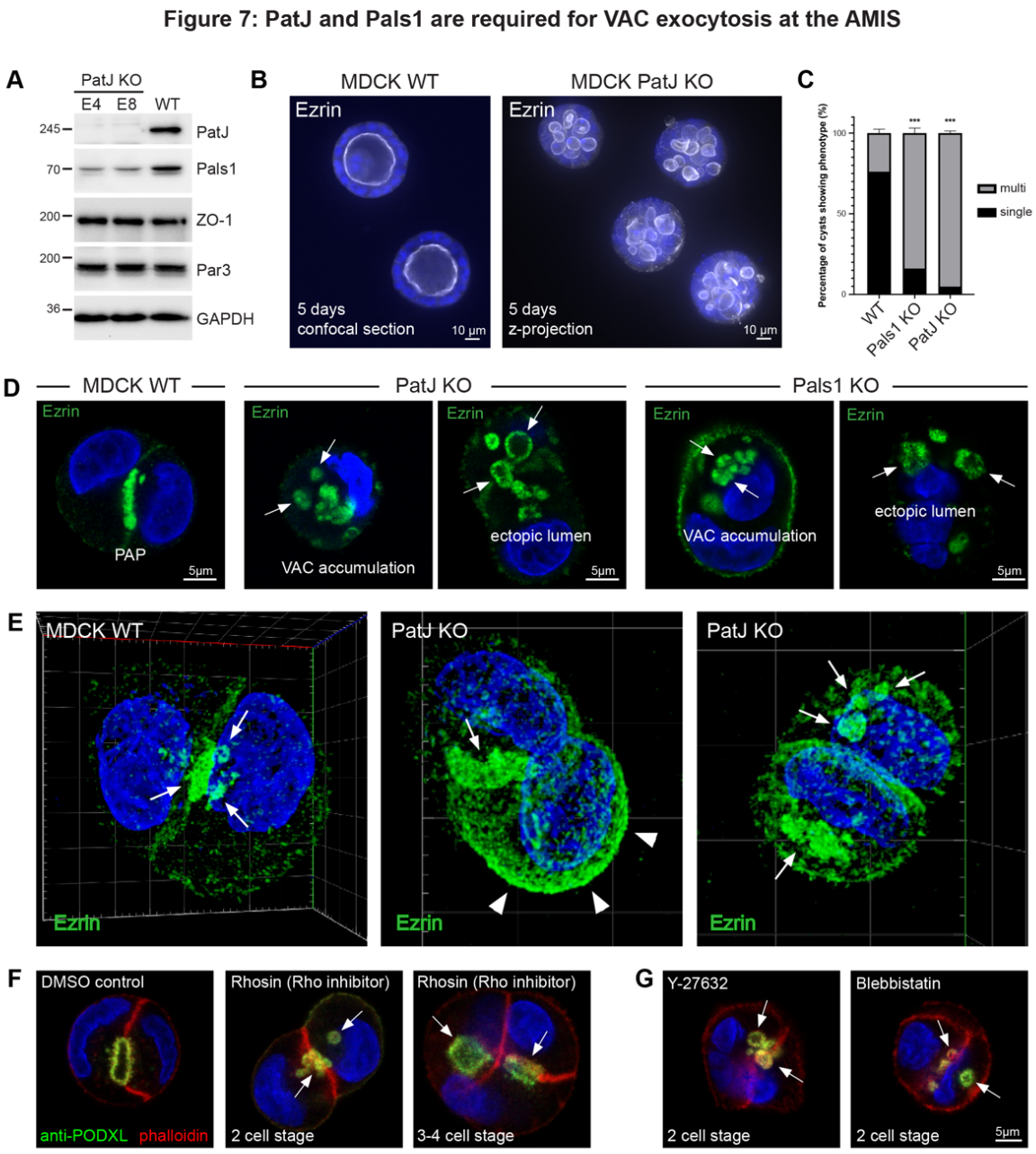

Figure 7: PatJ and Pals1 are required for VAC exocytosis at the AMIS
(A) Western blot analysis of PatJ KO MDCK clones E4 and E8 using the indicated antibodies. Note that Pals1 levels are decreased in PatJ KO cells.
(B) Representative confocal images of WT MDCK cysts and PatJ KO MDCK cysts embedded in Matrigel for 5 days. Cysts were stained with anti-ezrin antibody. The PatJ KO cysts are shown as maximum intensity z-projections.
(C) Quantification of the data shown in (B). Cyst phenotypes (single or multi-lumen) were quantified from three independent experiments. (n ~100 cysts each, error bars represent mean ± SEM, ***$p \leq 0.001$).
(D) Representative Airyscan images of WT MDCK cells, PatJ KO cells, and Pals1 KO cells embedded in Matrigel for 24h. Cells were stained with anti-ezrin antibody. Note the accumulation of ezrin in intracellular VACs and the formation of ectopic lumens in PatJ and Pals1 KO cells (white arrows).

(E) Representative 3D SIM reconstructions of WT MDCK cells and PatJ KO cells embedded in Matrigel for 24h. Cells were stained with anti-ezrin antibody. Note that ezrin accumulates in intracellular VACs (white arrows) and at the ECM-facing plasma membrane (white arrowheads) in PatJ KO cells.
(F) MDCK cells embedded in Matrigel for 16h were incubated with anti-PODXL antibody for 2h, followed by washout. Cells were left untreated (DMSO control) or treated for 6h with the Rho inhibitor Rhosin (20 μM). Cells were fixed, permeabilised, and stained with Phalloidin and secondary antibody.
(G) Experiment as in (F) except that cells were grown in the presence of the ROCK inhibitor Y-27632 (20 μM) or the myosin-II inhibitor Blebbistatin (50 μM).

Figure 8: PatJ controls the organisation of the apical cell cortex

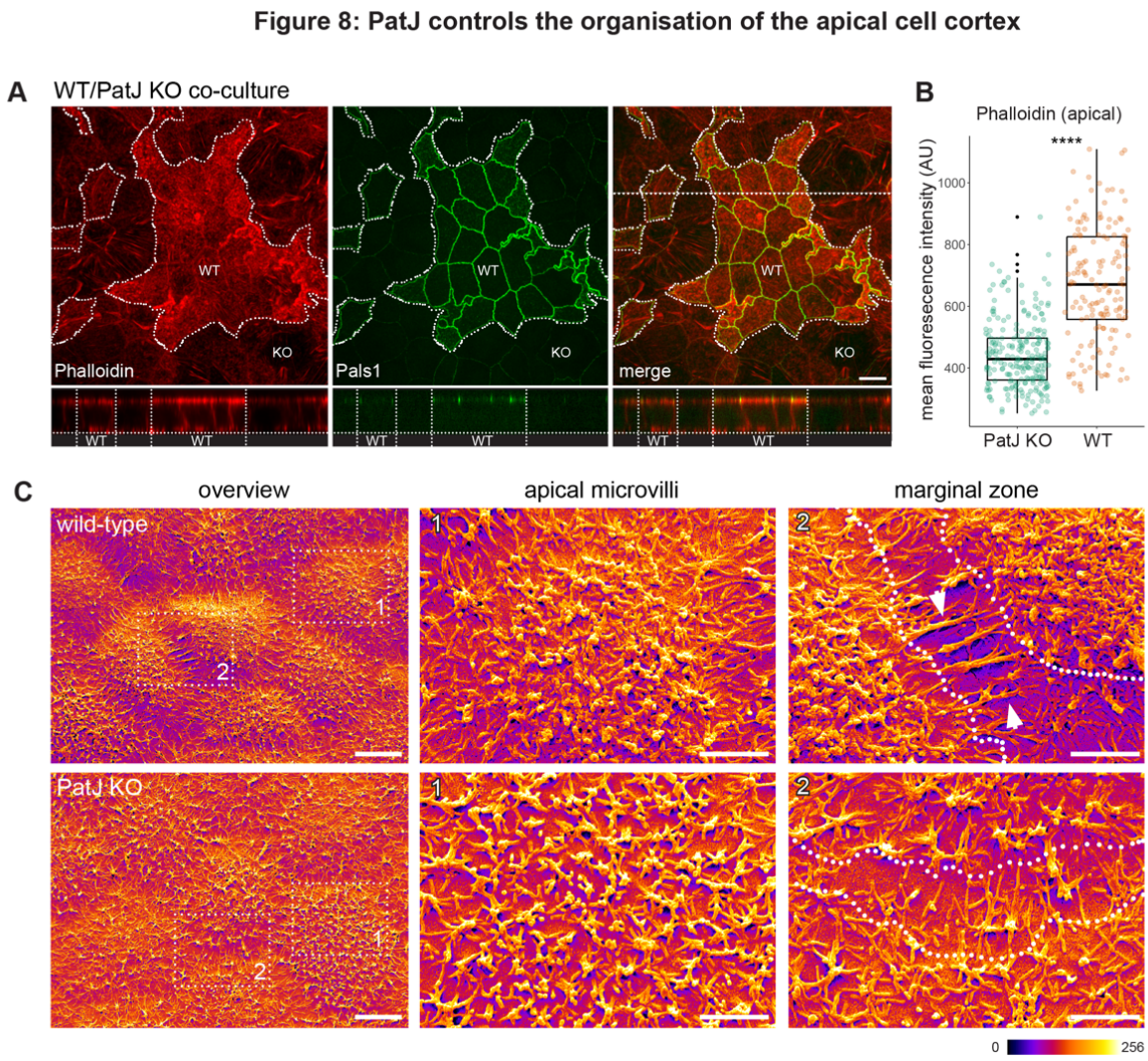

Figure 8: PatJ controls the organisation of the apical cell cortex
(A) MDCK WT cells and PatJ KO cells were co-cultured in a 1:1 ratio on Transwell filters for 12 days. Cells were fixed and stained with anti-PatJ antibodies and phalloidin. Representative x/y and x/z slices of confocal micrographs are shown. Scale bar 10 µm.
(B) Quantification of data shown in (A) using maximum intensity projections generated from the apical portion of the z-stack. **** $p<0.0001$; student's t-test (PatJ KO, n=226 cells; WT, n=152 cells).
(C) MDCK WT and PatJ KO cells were cultured on Transwell filters for 16 days and processed for SEM. Representative micrographs are shown in the "fire" look up table color code. Note the distinct organization of apical microvilli and junctional cross-bridges in the marginal zone of WT and PatJ KO cells. Scale bar 5 µm in the overview and 2 µm in the magnified images.